Tropospheric Aerosol Optical Thickness from the GOCART Model and Comparisons with Satellite and Sun Photometer Measurements

MIAN CHIN,*,+ PAUL GINOUX,*,+ STEFAN KINNE,+,# OMAR TORRES,+,# BRENT N. HOLBEN,+ BRYAN N. DUNCAN,@ RANDALL V. MARTIN,@ JENNIFER A. LOGAN,@ AKIKO HIGURASHI,& AND TERUYUKI NAKAJIMA**

**School of Earth and Atmospheric Sciences, Georgia Institute of Technology, Atlanta, Georgia*
+NASA Goddard Space Flight Center, Greenbelt, Maryland
#JCET, University of Maryland Baltimore County, Baltimore, Maryland
@Department of Earth and Planetary Sciences, Harvard University, Cambridge, Massachusetts
&National Institute for Environmental Studies, Tsukuba, Japan
***Center for Climate System Research, University of Tokyo, Tokyo, Japan*

(Manuscript received 16 January 2001, in final form 2 July 2001)

ABSTRACT

The Georgia Institute of Technology–Goddard Global Ozone Chemistry Aerosol Radiation and Transport (GOCART) model is used to simulate the aerosol optical thickness τ for major types of tropospheric aerosols including sulfate, dust, organic carbon (OC), black carbon (BC), and sea salt. The GOCART model uses a dust emission algorithm that quantifies the dust source as a function of the degree of topographic depression, and a biomass burning emission source that includes seasonal and interannual variability based on satellite observations. Results presented here show that on global average, dust aerosol has the highest τ at 500 nm (0.051), followed by sulfate (0.040), sea salt (0.027), OC (0.017), and BC (0.007). There are large geographical and seasonal variations of τ, controlled mainly by emission, transport, and hygroscopic properties of aerosols. The model calculated total τs at 500 nm have been compared with the satellite retrieval products from the Total Ozone Mapping Spectrometer (TOMS) over both land and ocean and from the Advanced Very High Resolution Radiometer (AVHRR) over the ocean. The model reproduces most of the prominent features in the satellite data, with an overall agreement within a factor of 2 over the aerosol source areas and outflow regions. While there are clear differences among the satellite products, a major discrepancy between the model and the satellite data is that the model shows a stronger variation of τ from source to remote regions. Quantitative comparison of model and satellite data is still difficult, due to the large uncertainties involved in deriving the τ values by both the model and satellite retrieval, and by the inconsistency in physical and optical parameters used between the model and the satellite retrieval. The comparison of monthly averaged model results with the sun photometer network [Aerosol Robotics Network (AERONET)] measurements shows that the model reproduces the seasonal variations at most of the sites, especially the places where biomass burning or dust aerosol dominates.

1. Introduction

Aerosols play important roles in global climate change. They affect earth's radiative budget by scattering or absorbing radiation and by altering cloud properties. The magnitude of these effects, however, is poorly constrained, because we have a limited knowledge of the processes that control the distributions as well as the physical, chemical, and optical properties of aerosols. Indeed, aerosol radiative forcing is one of the largest sources of uncertainty in climate change assessment (Houghton et al. 1995).

In the past 20 yr, aerosol distributions and properties have been measured by many space- and ground-based monitoring programs and intensive field campaigns. While field measurements offer detailed observations of aerosol composition and properties, they are usually limited in temporal or spatial coverage. In contrast, satellite observations provide extensive temporal and spatial coverage, but they are short on measurable quantities such as vertical profiles and aerosol compositions. Neither field measurements nor satellite observations alone would be sufficient to fully describe the aerosol distributions and its physical, chemical, and optical properties. Therefore, the use of global models becomes critical in integrating the satellite and in situ measurements. On the other hand, the model has to be evaluated by observations before we can place confidence in such a model. A common variable to link the model and measurements is the aerosol optical thickness, which is the most comprehensive quantity we can use to infer the

Corresponding author address: Mian Chin, NASA Goddard Space Flight Center, Code 916, Greenbelt, MD 20771.
E-mail: chin@rondo.gsfc.nasa.gov

aerosol burden and is generally available as a standard product of satellite retrievals as well as a commonly measured quantity in the field experiments.

Here we present a global simulation of aerosol optical thickness τ from the Georgia Institute of Technology–Goddard Global Ozone Chemistry Aerosol Radiation and Transport (GOCART) model. The model includes major tropospheric aerosol types of sulfate, dust, organic carbon (OC), black carbon (BC), and sea salt aerosols, providing global distributions of aerosol concentrations, vertical profiles, and optical thickness of individual as well as total aerosols. The information entailed here cannot be easily obtained from either satellite retrievals or field measurements but are key to estimating the magnitude of aerosol climate forcing.

Our study presented here has some similarities with, but also a number of major differences from, two previous global model studies. In their initial attempt using global models to estimate tropospheric aerosol composition, Tegen et al. (1997) had combined the results of individual aerosol types from different global general circulation models. More recently, Takemura et al. (2000) simulated all major types of tropospheric aerosol using a ''nudged'' general circulation model. Results of the two studies were compared with satellite observations from the Advanced Very High Resolution Radiometer (AVHRR) over the ocean and sun photometer measurements at a few surface sites. In our study, we have used a factor of 8–10 higher spatially resolved model and assimilated meteorological data. We have incorporated the most recent and much improved aerosol sources, especially dust and biomass burning emissions. Our results are compared with the very recent satellite retrieval of aerosol optical thickness from the Total Ozone Mapping Spectrometer (TOMS; Torres et al. 2002) over both land and ocean, and with two different AVHRR retrieval products (Stowe et al. 1997; Higurashi et al. 2000) over the ocean. In addition, sun photometer measurements at 20 sites over the globe from the Aerosol Robotic Network (AERONET; Holben et al. 2001) are used in this study to judge the model performance. These extensive comparisons not only provide the evaluation of the model, but also reveal the problems associated with both the model and satellite products and the methods of comparing these products.

In the following sections, we describe the individual aerosol components simulated in the model (section 2) and the method of calculating aerosol optical thickness τ (section 3). The global distributions of aerosol mass and τ are then presented (section 4), and the seasonal variations of τ are compared with the satellite products from TOMS and AVHRR (section 5) and with the sun photometer measurements from the AERONET sites (section 6). Finally, we discuss the difficulties and problems (section 7) and conclude with a summary of the results from this study (section 8).

2. Aerosol components simulated in the GOCART model

a. General

The GOCART model simulates major tropospheric aerosol types, including sulfate, dust, OC, BC, and sea salt aerosols. Detailed description of most of the model components has been presented in our previous work (Chin et al. 2000a; Ginoux et al. 2001); here we give a brief summary. The model has a horizontal resolution of 2° latitude by 2.5° longitude and 20–30 vertical sigma layers, and uses the assimilated meteorological fields generated from the Goddard Earth Observing System Data Assimilation System (GEOS DAS). The GEOS DAS fields are model-assimilated global analyses constrained by meteorological observations, with extensive prognostic and diagnostic fields archived for chemistry transport model applications (Schubert et al. 1993). These fields include winds, temperature, pressure, specific humidity, convective cloud mass flux, cloud fraction, precipitation, boundary layer depth, surface winds, and surface wetness that are used in the aerosol simulations. The GOCART model contains the following modules in aerosol simulation: emission, which includes sulfur, dust, black carbon, organic carbon, and sea salt emissions; chemistry, which currently uses prescribed OH, H_2O_2, and NO_3 fields for gaseous sulfur oxidations; advection, which is computed by a flux-form semi-Lagrangian method (Lin and Rood 1996); boundary layer turbulent mixing, which uses a second-order closure scheme (Helfand and Labraga 1988); moist convection, which is calculated using archived cloud mass flux fields (Allen et al. 1996); dry deposition, which includes gravitational settling as a function of aerosol particle size and air viscosity (Fuchs 1964) and surface deposition as a function of surface type and meteorological conditions (Wesely 1989); and wet deposition, which accounts for the scavenging of soluble species in convective updrafts and rainout/washout in large-scale precipitation (Giorgi and Chameides 1986; Balkanski et al. 1993).

Table 1 summarizes the global budget of each aerosol type in 1990, 1996, and 1997. For these 3 yr the model results are compared with the satellite and sun photometer measurements in this paper. It should be pointed out that the anthropogenic emission rates (i.e., fossil fuel and biofuel combustion) have been kept the same for each year, but they change with season to reflect the variation in energy use (Chin et al. 2000a). In contrast, biomass burning, volcanic, dust, and oceanic emissions are different each year. The emission height is determined by source type: dust and oceanic emissions are treated as surface sources; anthropogenic emissions are divided into those below 100 m and those above 100 m, based on the Global Emission Inventory Activity SO_2 emission data (http://weather.engin.umich.edu/geia); biomass burning emissions are evenly distributed throughout the boundary layer; and volcanic emissions

TABLE 1. Global budget of sources, sinks, atmospheric loading, and lifetimes of different types of aerosols.

Aerosol type		Total source[a] (Tg M yr^{-1})	Dry deposition[a] (Tg M yr^{-1})	Wet scavenging[a] (Tg M yr^{-1})	Total mass loading[a] (Tg M)	Lifetime (days)
Sulfate[b]	1990	39.5	4.9	34.6	0.63	5.8
	1996	39.2	4.7	34.5	0.68	6.3
	1997	39.2	4.6	34.6	0.65	6.1
OC[c]	1990	100.6	19.2	80.9	1.3	4.7
	1996	102.6	21.7	80.6	1.5	5.3
	1997	108.8	19.8	88.7	1.5	5.1
BC[c]	1990	17.5	3.8	13.7	0.28	5.7
	1996	17.8	4.2	13.6	0.31	6.3
	1997	18.7	3.9	14.8	0.32	6.2
Dust	1990	1830	1610	230	34	6.6
	1996	1600	1450	160	31	6.6
	1997	1520	1390	160	21	5.1
Sea salt	1990	5810	5740	66	7.9	0.5
	1996	7560	7450	88	12	0.6
	1997	7480	7420	68	14	0.7

[a] Unit: Tg M is 10^{12} g mass, which is Tg-S for sulfate, Tg-C for BC and OC.

[b] Sulfate: source includes 3.3 Tg-S yr^{-1} from direct emission and the rest is from SO_2 oxidation. Sulfate source should not be confused with its precursor (SO_2 and DMS) source shown in Fig. 1, which is about 94 Tg-S yr^{-1} (Chin et al. 2000a). The total source here is slightly different from that in Chin et al. (2000a) due to a minor correction in anthropogenic emission.

[c] OC and BC: sources include fuel combustion (6.5 Tg-C yr^{-1} for BC, 10.5 Tg-C yr^{-1} for OC), terpene oxidation (12.7 Tg-C yr^{-1} for OC), and biomass burning (the rest, varying from year to year).

are injected into a layer whose height and thickness is estimated based on the magnitude of the eruption and the altitude of the volcano (Chin et al. 2000a). The annual emissions for total sulfur, carbonaceous (BC + OC), dust, and sea salt in 1990 are shown in Fig. 1. In the following sections 2b–2e, we describe the sources for each aerosol component used in the model.

b. Sulfate

Among the various types of tropospheric aerosols, sulfate has probably the largest fraction of anthropogenic components. Sulfate is mainly formed in the atmosphere from the oxidation of SO_2, which is emitted dominantly from fuel combustions and industrial activities. A fraction of SO_2 is also released from biomass burning and volcanic eruptions. Anthropogenic emissions from fossil fuel and biofuel combustion are taken from the Emission Database for Global Atmospheric Research (Olivier et al. 1996). Emissions from biomass burning are scaled to the seasonal variation of burned biomass data (B. Duncan et al., unpublished manuscript; see section 2d) and normalized to the annual total SO_2 biomass burning emission (Spiro et al. 1992). Volcanic emissions include both continuously erupting volcanoes (Andres and Kasgnoc 1998) and sporadically erupting volcanoes (Simkin and Siebert 1994; Bluth et al. 1997). In addition to direct emission, about 14% of the SO_2 source in the model is from the oxidation of dimethylsulfide (DMS), which is released from the ocean. DMS emission is calculated using an empirical formula (Liss and Merlivat 1986) as a function of seawater DMS concentrations (Kettle et al. 1999) and wind speed at 10 m. The 10-m wind speed data used in the model are satellite observations from the Special Sensor Microwave Imager (SSM/I; Atlas et al. 1996). Total emission of sulfur in year 1990 is estimated at 94 Tg-S yr^{-1} (Fig. 1), with 80% from human activities and 20% from natural sources.

Chemical reactions in the model include DMS oxidation by OH during the day and by NO_3 during the night to form SO_2, and SO_2 oxidation by OH in the gas phase and by H_2O_2 in the aqueous phase to form sulfate. The reaction rates are calculated using the prescribed oxidant fields from the IMAGES model (Müller and Brasseur 1995). We do not include the in-cloud oxidation of SO_2 by ozone because this reaction represents a minor sink of SO_2, and could only be important over the polluted regions when the cloud is basic ($pH > 7$), which is rarely the case. Total sulfate source in 1990 is 39.5 Tg-S yr^{-1} (Table 1), with 92% from DMS and SO_2 oxidation and 8% from direct emission. Detailed description of sulfate simulation and comparisons with field measurements are presented elsewhere (Chin et al. 2000a,b).

c. Dust

Dust simulation in the GOCART model has been described in detail by Ginoux et al. (2001). Here, briefly, a new approach has been used in the GOCART model to identify the dust source. A dust-source function is constructed as the probability of sediments accumulated in the topographic depression regions with bare surfaces. In general, the deeper the depression is, the higher the probability of sediments accumulation will be. It has been found that this new approach has successfully located all the major dust sources including the Sahara and Sahel in Africa, the Taklimakan and Gobi Desert in China and Mongolia, the Arabia Desert, the dried lake basin in Australia, and other sources in southern Africa and South America (Ginoux et al. 2001). These

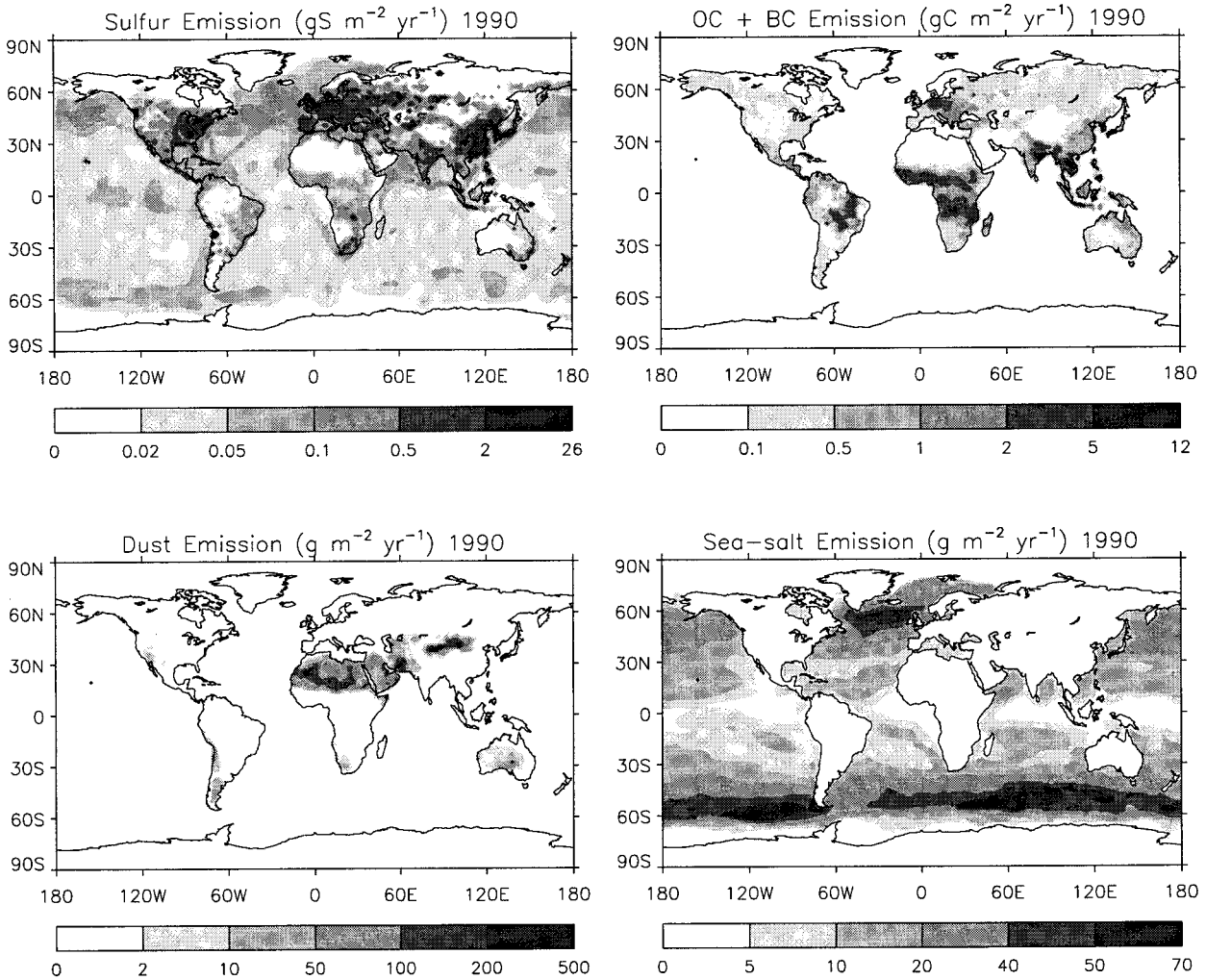

FIG. 1. Global annual emission rates for total sulfur (SO_2 + DMS) (g-S m^{-2} yr^{-1}), dust (g m^{-2} yr^{-1}), OC + BC (g-C m^{-2} yr^{-1}), and sea salt (g m^{-2} yr^{-1}) for 1990.

sediments can be readily uplifted into the atmosphere. The emission of dust is then calculated from the source function, surface wind speed, and surface wetness.

Dust particles ranging from 0.1 to 6 μm in radius are considered in the model. Larger particles are not included due to their very short lifetime, and thus limited significance in global scale (Tegen and Fung 1994). Seven size bins are assumed with particle radius of 0.1–0.18, 0.18–0.3, 0.3–0.6, 0.6–1, 1–1.8, 1.8–3, and 3–6 μm, following Tegen and Lacis (1996). The emission flux F_p (μg m^{-2} s^{-1}) for a size group p is expressed as

$$F_p = C \times S \times s_p \times u_{10}^2 \times (u_{10} - u_t), \quad \text{if } u_{10} > u_t,$$

where C is a dimensional factor (1 μg s^2 m^{-5}), S is the probability-source function described above, s_p is the fraction of size group p within the soil (Tegen and Fung 1994), u_{10} is the 10-m wind speed (m s^{-1}), and u_t is the threshold velocity of wind erosion determined by particle size and surface wetness (Ginoux et al. 2001). The annual dust emission in Table 1 varies from 1830 Tg yr^{-1} in 1990 to 1520 Tg yr^{-1} in 1997, determined mainly by the u_{10} at the source region.

d. Organic carbon and black carbon

The most important source of OC and BC is from biomass burning. In this study, emissions of OC and BC are calculated from a global 1° × 1° database of seasonal and interannual variability in burned biomass-based on satellite observations (B. Duncan et al., unpublished manuscript). In that database, the seasonal variation of biomass burning was determined as follows. First, a global 1° × 1° annual mean burned biomass inventory was used with a total of 5510 Tg yr^{-1} (Lobert et al. 1999; R. Yevich and J. Logan, 2000, personal communication). Second, for each 1° × 1° gridbox, the fraction of biomass burned in a particular month was determined by comparing the satellite-observed fire-

counts in that month with the annual mean number of fire-counts in that gridbox. The fire-count data were obtained from the Along Track Scanning Radiometer-2 (Arino and Rosaz 1999) and AVHRR (Arino and Melinotte 1995). Third, the monthly amount of biomass burned for each $1° \times 1°$ gridbox was determined by scaling the annual inventory to the corresponding fraction. Interannual variability was also determined using fire-counts from 1996 to 1999 on a $1° \times 1°$ grid and the TOMS absorbing aerosol index at the regional scale (B. Duncan et al., unpublished manuscript).

Using the above database, we have calculated the seasonal and interannual biomass burning emissions of BC and OC in this study from the estimated emission factors. The emission factor for BC from biomass burning was reported as from 1 to 2.2 g kg^{-1} dry mass burned for several types of vegetation (Patterson et al. 1986; Andreae et al. 1988). Here we assume an emission factor of 2 g kg^{-1} for BC for all vegetation types that are burned. We also assume a factor of 7 as the OC:BC emission ratio, which is within the range of 6.9 to 8.2 used by Liousse et al. (1996). Total annual biomass burning emissions of BC and OC are estimated at 11 and 77 Tg yr^{-1}, respectively, as climatologically averaged values. These values are a factor of 1.7–2 higher than the ones obtained by Liousse et al. (1996; 5.63 Tg yr^{-1} for BC and 44.6 Tg yr^{-1} for OC) and Cooke and Wilson (1996; 5.98 Tg yr^{-1} for BC). The most significant improvement of biomass burning emission in this study is in the seasonal cycle and the interannual variability, thanks to the use of a database that incorporates remotely sensed information (B. Duncan et al, unpublished manuscript). For example, total biomass burning emissions in October 1997 are 120% higher than the climatological emission value for October, due to the intensive biomass burning activity over Indonesia during that period of time.

Anthropogenic emissions of BC and OC are taken from the global dataset (Cooke et al. 1999) that includes emissions from domestic, transportation, and industrial combustion of various fuel types based on the fuel consumption statistics and emission factors of BC and OC. Annual emissions of BC and OC from anthropogenic sources are 6.4 and 10.5 Tg yr^{-1}, respectively. In addition to direct emissions, production of OC aerosol from a terrestrial source is estimated from the volatile organic compounds emission inventory (Guenther et al. 1995), assuming that 10% of these organic compounds are converted to OC aerosol (J. Penner 2000, personal communication). This secondary OC aerosol source is 12.7 Tg yr^{-1}.

Following Cooke et al. (1999), we assume that 80% of BC and 50% of OC emitted are hydrophobic, the rest being hydrophilic. The hydrophobic carbonaceous aerosols undergo aging processes to become hydrophilic in an *e*-folding time of 1.2 days. The atmospheric lifetime of carbonaceous aerosols is governed by dry deposition (for both hydrophilic and hydrophobic aerosols) and wet scavenging (for hydrophilic aerosols). The lifetime is about 5 days for OC and 6 days for BC (Table 1), similar to that estimate by Cooke et al. (1999; 4.5 days for OC, 5.3 days for BC).

e. Sea salt

Similar to dust uplifting, sea salt emissions from the ocean are highly dependent on the surface wind speed. We calculate the sea salt emission flux, F (particles m^{-2} s^{-1}), as a function of wind speed at 10 m, u_{10} (m s^{-1}) and the sea salt particle radius r (μm) using the empirical relationships from Gong et al. (1997) and Monahan et al. (1986):

$$dF/dr = 1.373u_{10}^{3.41}r^{-3}(1 + 0.057r^{1.05})10^{1.19\exp(-B^2)},$$

where $B = (0.380 - \log r)/0.65$. This formula has been found to produce reasonably well the sea salt emission rates for particles down to 0.1-μm radius in size (Gong et al. 1997). We include four size bins for sea salt with radius of 0.1–0.5, 0.5–1.5, 1.5–5, and 5–10 μm. The 10-m winds are from the satellite observations of SSM/I (see section 2b). As shown in Fig. 1, most sea salt is emitted at high latitudinal bands between 40° and 60° in both hemispheres due to strong winds. In contrast, very low sea salt emission rates are calculated in the tropical regions.

Once released into the atmosphere, sea salt aerosols are subject to transport, dry deposition, gravitational settling, and wet deposition. Because of their relatively large sizes and fast growth with ambient relative humidity (see next section), sea salt particles are removed quickly from the atmosphere with an averaged lifetime of 0.6 days.

3. Aerosol optical thickness

Given the model-simulated atmospheric distributions and composition of aerosols, the aerosol optical thickness (τ) can be calculated from the complex refractive indices, size distributions, and hygroscopic properties of aerosols. We assume lognormal size distributions for sulfate, OC, and BC aerosols as well as for each dust and sea salt bin. It has been shown that one key parameter best related to the radiative properties of a given size distribution is the cross section weighted effective radius r_e (Hansen and Travis 1974; Lacis and Mishchenko 1994), which is defined as $r_e = \int_r r\pi r^2 f(r)\, dr / \int_r \pi r^2 f(r)\, dr$, where $f(r)$ is the fraction of particles with radius between r and $r + dr$. The general relationship between the aerosol extinction optical thickness τ and the aerosol mass loading per unit area M can be expressed as (e.g., Lacis and Mishchenko 1994; Tegen and Lacis 1996),

$$\tau = \frac{3QM}{4\rho r_e}, \tag{1}$$

where ρ is the particle density, r_e is the effective radius

TABLE 2. Particle density, modal and effective radii (r_m and r_e), geometric std dev (σ_g) in lognormal size distribution, and the extinction coefficient (Q) and refractive indices at 500 nm for dry aerosols.

Aerosol type	Density (g cm^{-3})	r_m (μm)	r_e (μm)	σ_g (μm)	Q at 500 nm	Refractive index at 500 nm
Sulfate*	1.7	0.0695	0.156	2.03	1.343	$1.43 - 10^{-8}i$
OC*	1.8	0.0212	0.087	2.20	0.680	$1.53 - 0.005i$
BC*	1.0	0.0118	0.039	2.00	0.557	$1.75 - 0.45i$
Dust	2.6	0.0421	0.14	2.00	1.298	$1.53 - 0.0078i$
	2.6	0.0722	0.24	2.00	2.201	$1.53 - 0.0078i$
	2.6	0.1354	0.45	2.00	2.768	$1.53 - 0.0078i$
	2.6	0.2407	0.80	2.00	2.682	$1.53 - 0.0078i$
	2.6	0.4212	1.40	2.00	2.421	$1.53 - 0.0078i$
	2.6	0.7220	2.40	2.00	2.277	$1.53 - 0.0078i$
	2.6	1.3540	4.50	2.00	2.178	$1.53 - 0.0078i$
Sea salt	2.2	0.228	0.80	2.03	2.696	$1.50 - 1.55 \times 10^{-8}i$
	2.2	1.64	5.73	2.03	2.143	$1.50 - 1.55 \times 10^{-8}i$

* Assuming a maximum radius at 0.5 μm.

defined above, and Q is the extinction coefficient, which is calculated from the Mie-scattering theory using the aerosol size distribution and refractive index. Both τ and Q are wavelength-dependent.

The aerosol optical properties in this study are based on the Global Aerosol Data Set (GADS; Köpke et al. 1997). Table 2 lists the particle density, modal and effective radius, geometric standard deviation of the lognormal size distribution, and the extinction coefficient and complex refractive index at a commonly used reference wavelength of 500 nm for each aerosol type and size bin (dry). Here the sea salt aerosols are further grouped into accumulation-mode and coarse-mode size bins in order to be consistent with the GADS. We also assume that sulfate, OC, and BC are all submicron aerosols with a maximum radius of 0.5 μm. The Q values for dust in Table 2 are somewhat different from the ones in Tegen and Lacis (1996). Our values for dust particles with r_e smaller than 0.45 μm are 10%–15% lower than those in Tegen and Lacis (1996) but are 1%–5% higher for larger particles. This may be attributed to the different size distributions used between these two studies, as the gamma distributions were used by Tegen and Lacis (1996) while lognormal distributions are assumed in this study.

With the exception of dust, aerosols are considered to have different degrees of hygroscopic growth rate with ambient moisture. Table 3 shows the growth factors of particle radius $r_e/r_{e,\mathrm{dry}}$ for different aerosol types at ambient RH, based on the GADS data and the database compiled by d'Almeida et al (1991). The $r_e/r_{e,\mathrm{dry}}$ values in Table 3 are within the previously measured range for urban, rural, and maritime aerosols (Whitby 1984, and references therein). Under the humidification effects, all quantities in Eq. (1) change with RH for hygroscopic aerosols. For example, the aerosol mass M is the sum of dry mass M_d and the mass of water uptaken by the aerosol; the particle density ρ is the combination of the densities of dry aerosol ρ_d and water ρ_w, expressed as $\rho = f_d\rho_d + (1 - f_d)\rho_w$ with f_d being the volume fraction of dry aerosol within an aerosol particle. Similarly, the effective refractive index used in calculating Q is the combination of the refractive indices of water and dry aerosols. The most convenient way of linking the aerosol optical thickness and the aerosol dry mass M_d is to rearrange Eq. (1) into

$$\tau = \beta M_d, \tag{2}$$

where β is called specific extinction or mass extinction efficiency (m^2 g^{-1}), which is simply the quantities in the right-hand side of Eq. (1) divided by the dry aerosol mass M_d; that is,

$$\beta = \frac{3QM}{4\rho r_e M_d}, \tag{3}$$

so that all the humidification effects are embodied in the value of β.

TABLE 3. Hygroscopic growth factors of $r_e/r_{e,\mathrm{dry}}$ at different RH.

RH (%)	0	50	70	80	90	95	99
Sulfate	1	1.4	1.5	1.6	1.8	1.9	2.2
OC	1	1.2	1.4	1.5	1.6	1.8	2.2
BC	1	1.0	1.0	1.2	1.4	1.5	1.9
Sea salt	1	1.6	1.8	2.0	2.4	2.9	4.8

Figure 2 demonstrates the relative humidity and wavelength dependence of β for hygroscopic aerosols. Figure 2a shows that at 80% RH, the βs at 500 nm for sulfate, OC, and sea salt aerosols are about a factor of 2–3 greater than their dry values, whereas at 99% RH the βs are a factor of 10 greater for sulfate and OC, and about 20 for sea salt. For the hydrophilic BC, it starts growing only when RH $>$ 70%, and its β increases at a factor of 2.5 at 99% RH from the dry value. The β enhancement factors calculated here are consistent with those measured in the Tropospheric Aerosol Radiative Forcing Observational Experiment where a factor of 1.81–2.31 at wavelength of 550 nm was found as the ratio of light scattering efficiency at 80% RH to that at 30% (Kotchenruther et al. 1999). Figure 2b plots the

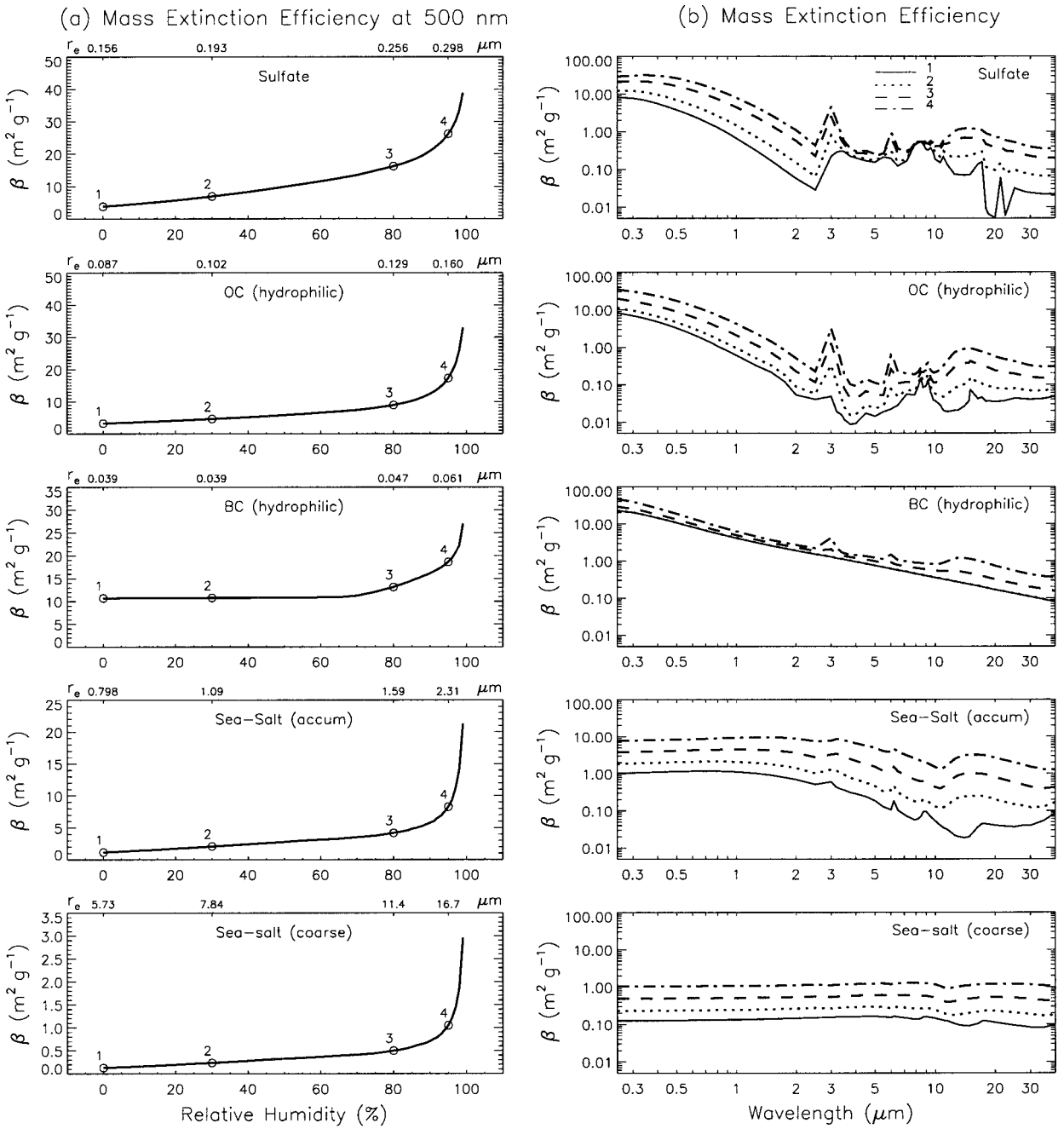

FIG. 2. Mass extinction efficiencies for hygroscopic aerosols (a) at wavelength of 500 nm as a function of RH; (b) as a function of wavelength for 4 different sizes corresponding to RH of 0% (line 1), 30% (line 2), 80% (line 3), and 95% (line 4). The r_e values are indicated at the top of each panel in Fig. 2a.

wavelength dependence of β for hygroscopic aerosols at four different sizes, corresponding to RH at 0%, 30%, 80%, and 95% (number and r_e for these sizes indicated in Fig. 2a). There is a strong decrease in β with the increase of wavelengths for sulfate, OC, and BC at UV and visible spectral regimes, in contrast with sea salt aerosol which shows little variation at those wavelengths due to its relatively large size. The more the water is taken up by the aerosol particles, the higher the extinction efficiency will become.

As mentioned earlier, we assume that the size of dust aerosols do not change with RH, since dust aerosols contain little hygroscopic material and their radiative properties are relatively insensitive to changes in RH (Li-Jones et al. 1999). Although studies have found that certain type of mineral (e.g., montmorillonite) could

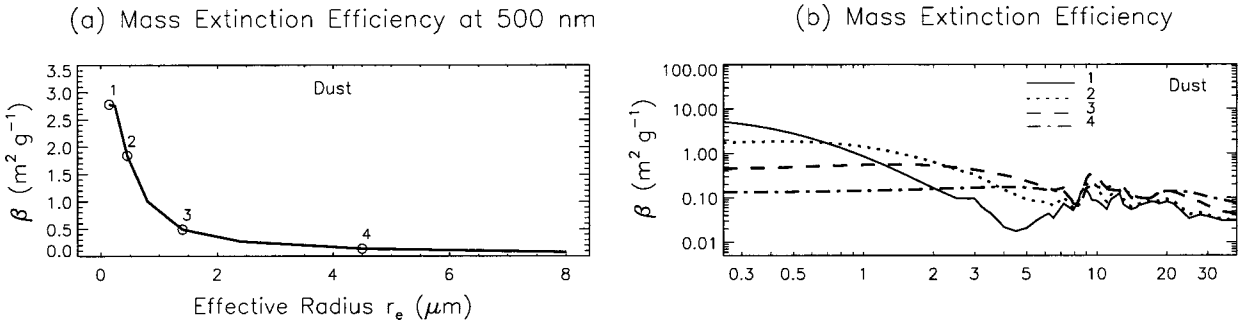

FIG. 3. Mass extinction efficiencies for dust aerosol (a) as a function of particle size; and (b) as a function of wavelength for four different sizes at r_e of 0.14 (line 1), 0.45 (line 2), 1.4 (line 3), and 4.5 μm (line 4). Sizes are indicated in (a).

take up some water at high RH (Grim 1968; I. Sokolik 2000, personal communication), it is not possible to estimate the hygroscopic growth rate of dust particles at the present time without a sufficient knowledge of the dust mineralogical composition. Therefore, for dust aerosols the β in Eq. (3) is just $3Q/(4\rho r_e)$. Figure 3 shows the β values for dust as a function of r_e (Fig. 3a) and wavelengths (Fig. 3b). The four sizes of dust particles in Fig. 3b are at $r_e = 0.14$, 0.45, 1.4, and 4.5 μm. At the UV and visible wavelengths the change of r_e dominates the change of Q (Table 2) so that the β decreases with the increase of r_e. However, because the smaller particles have a much stronger wavelength dependence, they become less efficient in light extinction than the larger particles at longer wavelengths (Fig. 3b).

4. Results

The model-simulated global distributions of aerosol dry mass loading M_d and optical thickness τ at a wavelength of 500 nm are shown in Fig. 4 in the left and middle column, respectively. These are annually averaged values for 1990 under all sky conditions (clear and cloudy). Here M_d and τ are column integrated values; that is, $M_d = \Sigma_k\, m_d(k)$ and $\tau = \Sigma_k\, \beta(k) m_d(k)$, where m_d is the aerosol dry mass per square meter at each model layer k, and β is the mass extinction efficiency, which is a function of RH(k) at the same layer. Figure 4 shows that the patterns are similar between M_d and τ, with the maximum values located near the aerosol source regions (Fig. 1). For example, sulfate aerosols are concentrated over Europe, eastern Asia, and eastern North America, whereas OC and BC are mostly concentrated at the biomass burning regions of Africa, Brazil, Southeast Asia, and Indochina. Maximum values of dust τ are found over Sahara and Taklimakan–Gobi Desert. Finally, high sea salt aerosol levels are located at high latitudinal bands near 60°S and 60°N, directly reflecting the high emission rates due to the strong surface winds at these locations. On the global average, dust aerosol has the highest optical thickness at 500 nm (0.051), followed by sulfate (0.040), sea salt (0.027), OC (0.017), and BC (0.007). Although BC is optically thin, it plays a crucial role in determining the magnitude of aerosol radiative forcing and the atmospheric heating rates (e.g., Haywood et al. 1997) because of its strong ability to absorb light.

The ratio of column-integrated τ and M_d can be viewed as the column effective mass extinction efficiency β, which is shown in the right column of Fig. 4. The effects of relative humidity are apparent from the β distributions for sulfate, OC and BC: the most obvious high humidity bands are located near 60°S, equator, and 60°N, in contrast with the two dry bands near 30°N and 30°S. The column effective β for dust reflects the relative abundance of the submicron and supermicron sizes, as smaller particles are more efficient in light extinction at 500 nm (Fig. 3). In general, the β is higher at locations further away from the dust source region, since larger particles are subject to more efficient dry deposition, hence shorter lifetimes, than smaller particles. The distribution of β for sea salt is also determined by the particle size, as well as by RH. The globally and annually (1990) averaged β values for bulk aerosols at wavelength of 500 nm are 11 $m^2\ g^{-1}$ for sulfate, 7 $m^2\ g^{-1}$ for OC, 12 $m^2\ g^{-1}$ for BC, 0.8 $m^2\ g^{-1}$ for dust, and 1 $m^2\ g^{-1}$ for sea salt.

If we assume that aerosols are externally mixed, that is, each aerosol particle contains only one type of aerosol, then the total aerosol optical thickness can be obtained as the sum of the τs of individual aerosol types. The modeled total τ at 500 nm in 1990 is shown in Fig. 5 (top panel). To understand the relative importance of each aerosol type, we also plot in Fig. 5 the percentage contributions of sulfate, carbonaceous (OC + BC), dust,

→

FIG. 4. Model-calculated annually averaged global distributions of column-integrated aerosol dry mass (left column), optical thickness at 500 nm at ambient RH (middle column), and column effective mass extinction efficiency at 500 nm (right column). Results are for 1990, under all sky conditions (clear and cloudy).

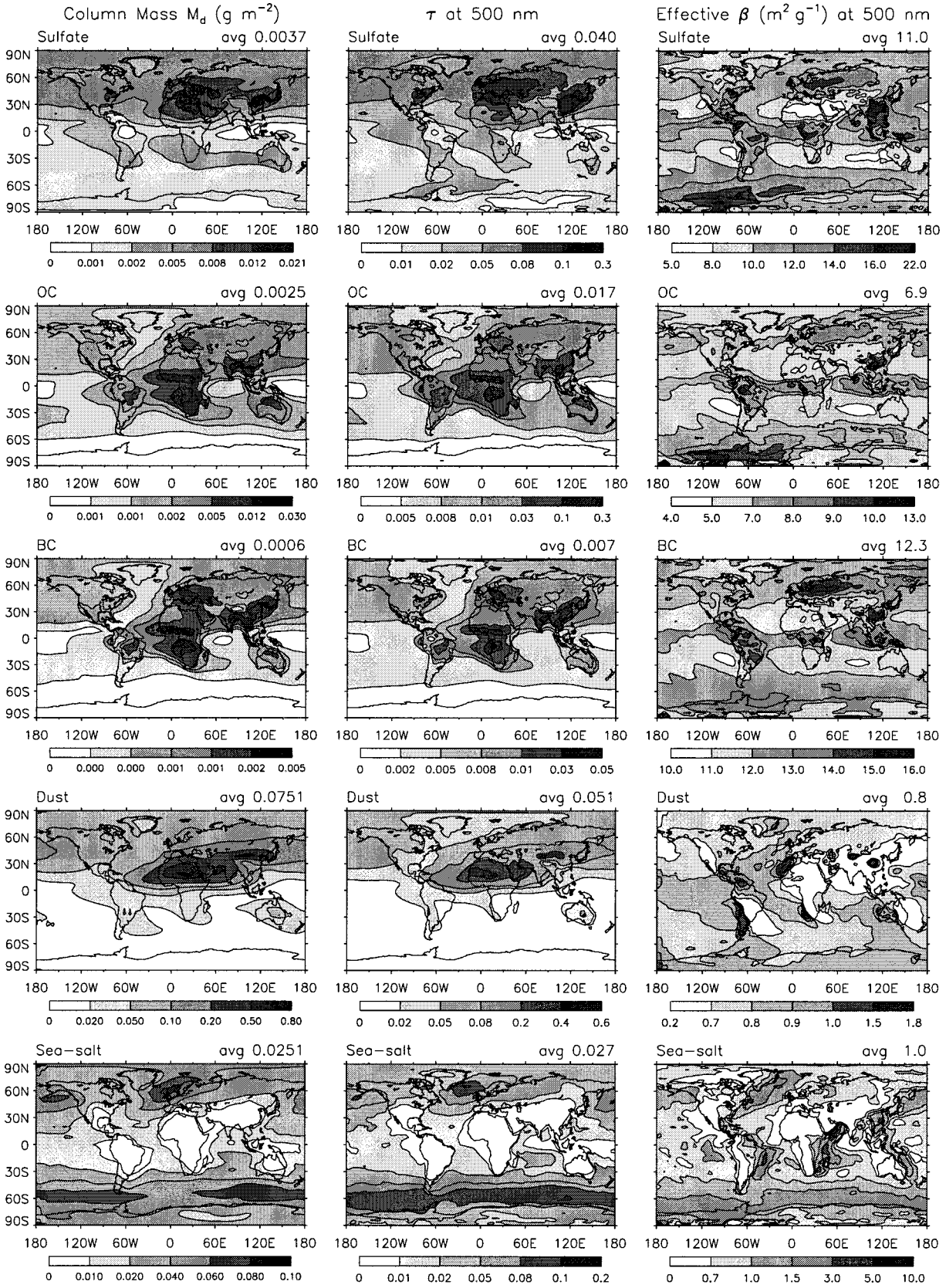
Column Mass M_d (g m^{-2})
τ at 500 nm
Effective β (m^2 g^{-1}) at 500 nm
Sulfate avg 0.0037
Sulfate avg 0.040
Sulfate avg 11.0
OC avg 0.0025
OC avg 0.017
OC avg 6.9
BC avg 0.0006
BC avg 0.007
BC avg 12.3
Dust avg 0.0751
Dust avg 0.051
Dust avg 0.8
Sea−salt avg 0.0251
Sea−salt avg 0.027
Sea−salt avg 1.0
90N 60N 30N 0 30S 60S 90S
180 120W 60W 0 60E 120E 180
0 0.001 0.002 0.005 0.008 0.012 0.021
0 0.01 0.02 0.05 0.08 0.1 0.3
5.0 8.0 10.0 12.0 14.0 16.0 22.0
0 0.001 0.001 0.002 0.005 0.012 0.030
0 0.005 0.008 0.01 0.03 0.1 0.3
4.0 5.0 7.0 8.0 9.0 10.0 13.0
0 0.000 0.000 0.001 0.001 0.002 0.005
0 0.002 0.005 0.008 0.01 0.03 0.05
10.0 11.0 12.0 13.0 14.0 15.0 16.0
0 0.020 0.050 0.10 0.20 0.50 0.80
0 0.02 0.05 0.08 0.2 0.4 0.6
0.2 0.7 0.8 0.9 1.0 1.5 1.8
0 0.010 0.020 0.040 0.060 0.080 0.10
0 0.01 0.02 0.05 0.08 0.1 0.2
0 0.7 1.0 1.5 3.0 5.0 10.0

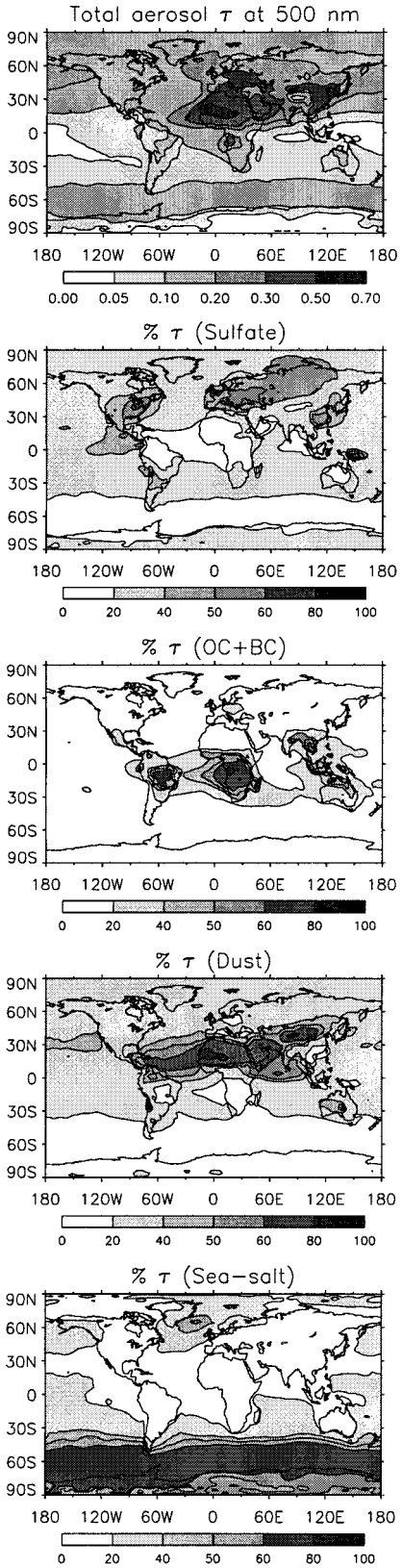

and sea salt to the total τ (lower four panels). Over major pollution regions of eastern North America, Europe, and eastern Asia, sulfate aerosol usually contributes 40%–60% to the total τ. Carbonaceous aerosols are the most important aerosol type over the biomass burning regions in Brazil, central and southern Africa, and southern Asia (with large seasonal variations). Dust aerosol is the most predominant aerosol over northern Africa, tropical North Atlantic, northern Indian Ocean, and northern China–Mongolia regions, where it contributes 60%–90% to the total τ. Sea salt aerosol, on the other hand, contributes the most to the τ (60%–80%) at the 45° to 75°S latitudinal band. It should be noted that there is a strong seasonal variation of the τ and the relative contributions from each aerosol type caused by the seasonal change in source strengths and transport pattern. In the next two sections, the total τ from the model is compared with that from the spaceborne and ground-based observations at different seasons.

5. Comparison with satellite retrievals from TOMS and AVHRR

Satellite measurements of aerosols are the only means of providing global or near-global coverage in space and time. Two of the satellite sensors, AVHRR and TOMS, have been measuring aerosol signal for more than 20 yr at either visible (AVHRR) or ultraviolet (TOMS) wavelengths. There are several retrieval algorithms to extract the aerosol optical thickness from the AVHRR-measured backscatter radiation, using either one-channel retrieval (Stowe et al. 1997) or two-channel retrieval technique (Nakajima and Higurashi 1998; Mishchenko et al. 1999; Higurashi et al. 2000). Because of the highly variable land surface reflectance of the visible wavelengths, the AVHRR retrieval cannot derive aerosol information over the land. In contrast, the retrieval products from the TOMS measurements cover both land and ocean, since the TOMS instrument measures backscattering at the UV wavelengths, which have low and nearly constant reflectance at most surfaces (Herman and Celarier 1997). The TOMS products, therefore, provide unique information of aerosol sources, which are all located over the land except sea salt. Aerosol products from the TOMS retrieval include aerosol index, which is the ratio of the backscatter signals from the two TOMS UV channels (Herman et al. 1997), and aerosol optical thickness at 380 nm (Torres et al. 2002).

←

FIG. 5. Model-calculated annually averaged total aerosol optical thickness at 500 nm (top panel) and the contributions (%) of individual aerosol component to the total optical thickness (panels 2–4). Results are for 1990, under all sky conditions (clear and cloudy).

a. Global distribution

We compare the seasonal variations of modeled total aerosol optical thickness with the TOMS data for 1997 (Fig. 6) and the AVHRR data for 1990 (Fig. 7). The TOMS data in Fig. 6 are at 550 nm, converted from the original 380 nm (Torres et al. 2002). Two different versions of the AVHRR products are shown in Fig. 7: one is the NOAA operational product from the one-channel (630 nm) retrieval algorithm (Stowe et al. 1997, hereafter AVHRR-1), while the other is from two-channel (630 and 840 nm) retrieval algorithm (Higurashi et al. 2000, herafter AVHRR-2). The AVHRR-2 data were converted to 500 nm (Higurashi et al. 2000). Table 4 summarizes some key parameters, including aerosol refractive index, size distribution, and cloud screen criteria, used in the TOMS and AVHRR retrievals. Because cloud screening algorithms in the satellite retrieval have rejected a large amount of raw data, the satellite data shown in Figs. 6 and 7 are monthly composite rather than monthly average.

Both the TOMS data and the model results (Fig. 6) show that the highest values of τ are persistently located over the northern Africa where dust is the predominant aerosol component, except in the biomass burning season (e.g., January) when carbonaceous aerosols are also important there. High dust τ values over the Taklimakan and Gobi Deserts in Asia and over the Arabian peninsula are also seen from the model, matching the locations of ''hot spot'' in the TOMS products. Transport of the aerosol plume from northern Africa to the Atlantic Ocean is the most visible feature from both the model and the satellite products (Figs. 6 and 7). During the burning seasons (e.g., July and October in Figs. 6 and 7), high τ values from biomass burning aerosols are also located at the west coast of southern Africa. Another feature from the model is the sea salt band near 60°S for all seasons, a feature that is particularly evident from the AVHRR-1 data. The model shows an interannual variability of τ between the two different years of 1990 and 1997 (first column in Figs. 6 and 7), with the most notable difference in October. While it is only 0.05–0.2 in 1990, the τ over Indonesia has reached values above 1 in 1997 due to the intensive biomass burning started in September. A similar τ value is also shown in the TOMS data for 1997 (Fig. 6). The modeled τ over the ocean in 1997 is also higher than that in 1990, largely a result of the higher sea salt emission in 1997 (Table 1).

One major discrepancy between the model and the satellite data is that the model has a much stronger latitudinal gradient over the ocean. The satellite data generally show little latitudinal contrast, but the model shows a band with minimum τ values over the southern tropical ocean between 0° and 30°S, typically a factor of 2–3 lower than the values at northern mid- and high latitudes. Such a latitudinal gradient is a common feature among most of the global aerosol models (see Penner et al. 2002). Difficulties in retrieving low τ values at remote ocean from the satellite measurements may explain the discrepancy (see discussions in section 7), although increasing sea salt or biogenic sulfur emissions at the southern tropical ocean in the model would reduce the gradient and bring a better match between the model results and the satellite data (Penner et al. 2002).

Figure 7 clearly reveals the discrepancy in the two AVHRR retrieval products. While the difference is small over the regions where τ values are relatively high, such as off the west coast of northern Africa, the τ over the remote oceans from AVHRR-1 is more than a factor of 2 lower than that from AVHRR-2. Although the τs are at 630 nm from AVHRR-1, which are expected to be slightly lower than those at 500 nm from AVHRR-2, the differences shown in Fig. 7 are much too large to be explained by the τs at different wavelengths. Differences in retrieval techniques and assumptions of aerosol properties (Table 3) are likely the cause of the differences in the two AVHRR products.

b. Regional comparison

To achieve a more quantitative comparison, we extract the model results and the satellite data from selected regions over the land and ocean (Fig. 8). These regions are chosen to represent source, outflow, or remote environment and with sufficient satellite coverage for all seasons. The eight land regions include three major pollution source regions (L1: United States, L2: Europe, L3: eastern Asia), two dust source regions (L4: northern Africa, L5: Asia), two biomass burning regions (L6: Brazil, L7: southern Africa), and Australia (L8). The eight ocean regions include those influenced by continental outflow (O1–O4), Saharan dust outflow (O5), biomass burning outflow (O6), and those at remote oceans (O7: southern Indian Ocean, O8: southern tropical Pacific). Note that O7 can be influenced by biomass burning aerosols (Fig. 5) during the burning seasons. Aerosol over the continental outflow regions is usually composed by several different types (Figs. 4 and 5), and the relative importance of individual type varies with the season. The regional comparisons are presented in Fig. 9 where the model results are compared with the TOMS (Figs. 9a,b) and AVHRR (Figs. 9c,d) data at similar wavelengths for the same time periods in Figs. 6 and 7. The comparison with AVHRR is limited to oceanic regions because there were no AVHRR retrievals over the land.

Figure 9a shows that the model and the TOMS data agree to within 25% over the major pollutions source regions (L1–L3) for all seasons, and to within 40% over the dust source regions (L4 and L5) except for January over northern Africa when the modeled τ is a factor of 2 higher than the TOMS data. Over the biomass burning regions (L6 and L7), the model agrees with the TOMS data to within 10%–50% during the burning seasons (July and October), but in the nonburning seasons the background τs from the model are four to five times

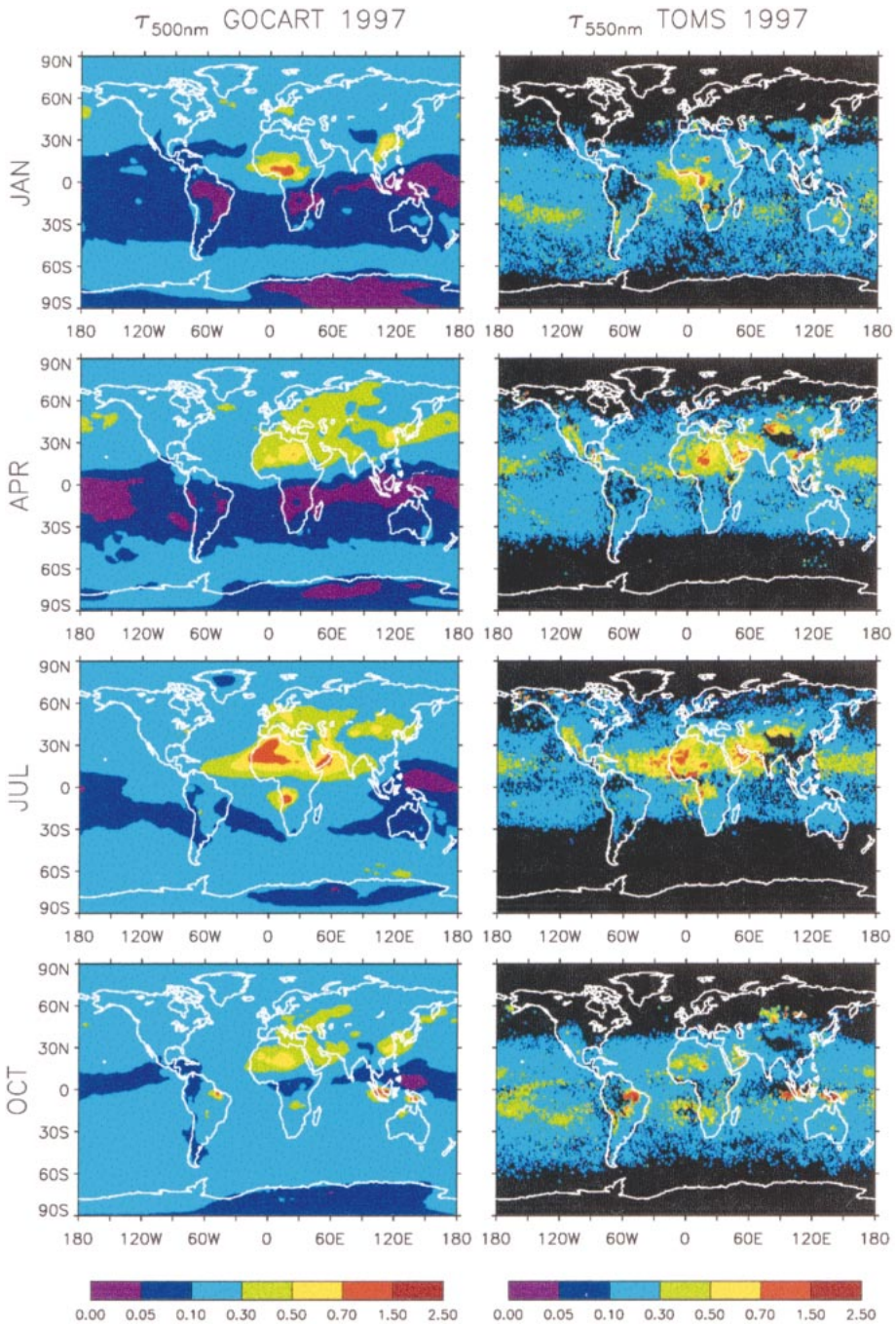

FIG. 6. Total aerosol optical thickness in Jan, Apr, Jul, and Oct 1997 from the GOCART model (left column) and the TOMS retrieval (right column). Model results are at wavelength of 500 nm, and the TOMS data are at 550 nm.

lower than those from the TOMS data. Over Australia (L8), the modeled τs are around 40% of the TOMS values except in October 1997 when, influenced by biomass burning emissions, the model and the TOMS agree.

Over the ocean, the modeled τs agree with both TOMS (Fig. 9b) and AVHRR-2 (Fig. 9d) to within 0%–40% at regions that are affected by continental (O1–O4) or dust outflow (O5). Over the biomass burning outflow region (O6), the discrepancy between the model and the satellite data is similar to that over the biomass burning source regions (L6 and L7): the modeled τs are two to five times smaller than the satellite data in the nonburning seasons, but the agreement is within 35%

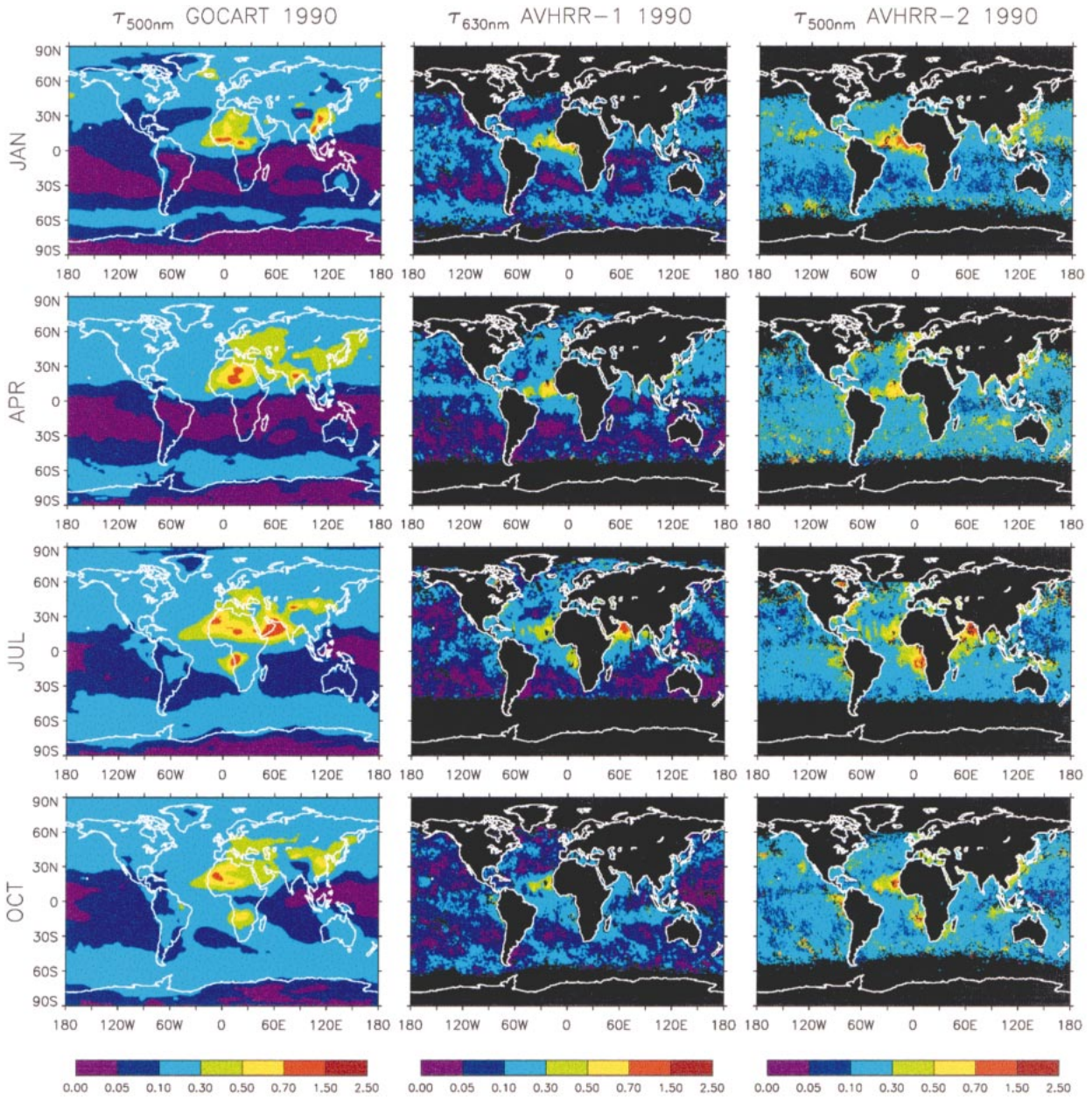

FIG. 7. Total aerosol optical thickness in Jan, Apr, Jul, and Oct 1990 from the GOCART model (left column), one-channel AVHRR retrieval or AVHRR-1 (middle column), and two-channel AVHRR retrieval or AVHRR-2 (right column). Both model results and AVHRR-2 data are at 500 nm, and AVHRR-1 data are at 630 nm.

during the burning season. The largest discrepancy between the model and the TOMS or AVHRR-2 lies, as we have seen in Figs. 6 and 7, at the remote oceanic regions in the Southern Hemisphere (O7 and O8), where the modeled τs are 0.05–0.15 in 1997 and 0.04–0.10 in 1990, which are two to five times lower than the τs from TOMS and AVHRR-2. This suggests that either the model has significantly underestimated aerosol source in the remote ocean, or the TOMS and AVHRR-2 retrievals have overestimated the background aerosol level due to the large uncertainties at low aerosol signals. In contrast, the lower τ from AVHRR-1 (Fig. 9c) retrieval brings a better agreement with the model results over the remote regions compared to AVHRR-2, but worsens over the continental outflow regions (O1–O4). In general, the model agrees better with AVHRR-1 than AVHRR-2 over the remote oceans, but the reverse is the case over the outflow regions.

The regional comparison is summarized in Fig. 10. We plot different symbols to separate results from major source and outflow region (closed symbols) with those over background regions (open symbols) to demonstrate

TABLE 4. Aerosol models and cloud screen methods used in the TOMS and AVHRR retrievals.

	TOMS	AVHRR-1	AVHRR-2
Retrieval wavelength	331 and 360 mm*	630 nm	630 and 840 nm
Aerosol type	A specific aerosol type (sulfate, carbon, or dust) or group selected based on the location and time	Marine (nonabsorbing)	Slightly absorbing
Refractive index	Sulfate: 1.43–0*i* Carbon: 1.55–0.15*i* to 1.55–0.55*i* Dust: 1.56–0.006*i*	1.4–0*i*	1.5–0.005*i*
Size distribution	Lognormal distribution for each aerosol type and group**	Single modal, lognormal distribution, r_m = 0.1 μm, σ_g = 2.03 μm	Bimodal lognormal distribution, r_m = 0.17, 3.44 μm, σ_g = 1.96, 2.75 μm
Cloud screening	Rejected pixels with reflectance greater than a threshold value**	Screened using pixel reflectance and brightness temperature value, ratio, difference, and spatial uniformity thresholds from multiple wavelengths	Screened using pixel reflectance and brightness temperature value, and spatial uniformity thresholds from multiple wavelengths

* These are the actual *Earth-Probe* TOMS (1996–present) channels. The retrieved τ is at 380 nm to be consistent with the long-term *Nimbus-7* TOMS (1978–1993) record (Torres et al. 2002).
** Details and actual values are given in Torres et al. (2002).

correlations between the model and the satellite data in different area. The modeled and TOMS τs at the land source regions are significantly correlated with a coefficient of 0.67, and the agreement is within a factor of 2 (Fig. 10a). Over the oceanic regions, which are influenced by the land outflow, the model results and the satellite data are also closely correlated with the correlation coefficients of 0.72, 0.84, and 0.75 with the TOMS (Fig. 10b), AVHRR-1 (Fig. 10c), and AVHRR-2 (Fig. 10d) data, respectively. The overall agreement is within a factor of 2, though the model results are lower than the TOMS and AVHRR-2 data but higher than the AVHRR-1 data. Over the remote regions or under ''background'' conditions (no major emissions), there are either no or very weak correlations between the model results and the satellite data. The model results are typically a factor of 2–5 lower than the TOMS and AVHRR-2 data over the remote regions, but agrees with AVHRR-1 data within a factor of 2. These comparisons demonstrate the limitations of quantitative evaluations of model results with the satellite data.

It has been reported that the latitudinal location of the aerosol plume at the tropical eastern Atlantic (off the western Africa coast) changes with seasons in the AVHRR data (e.g., Rao et al. 1988; Moulin et al. 1997), as the maximum value of τ is seen located near 10°N

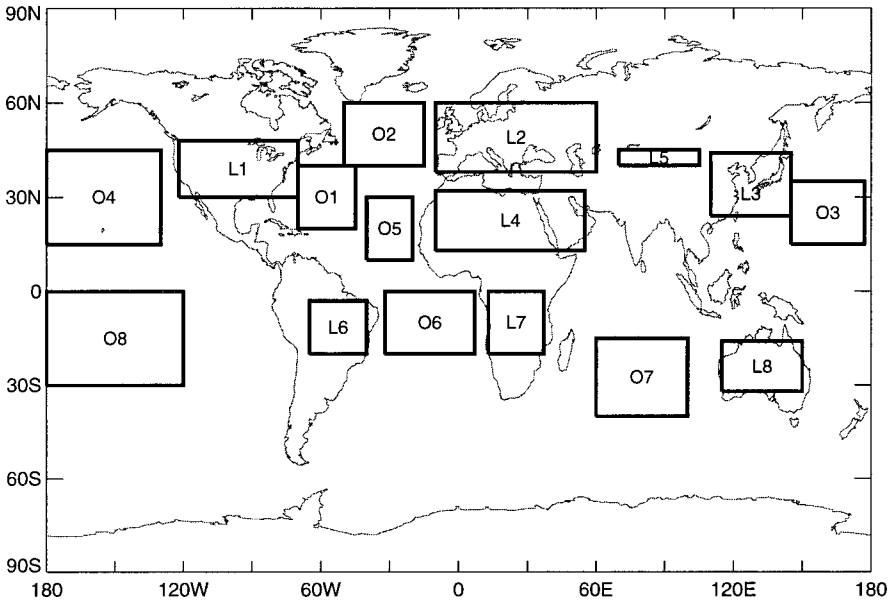

FIG. 8. Borders of eight land regions (L1–L8) and eight oceanic regions (O1–O8) in comparisons of model results and satellite retrievals.

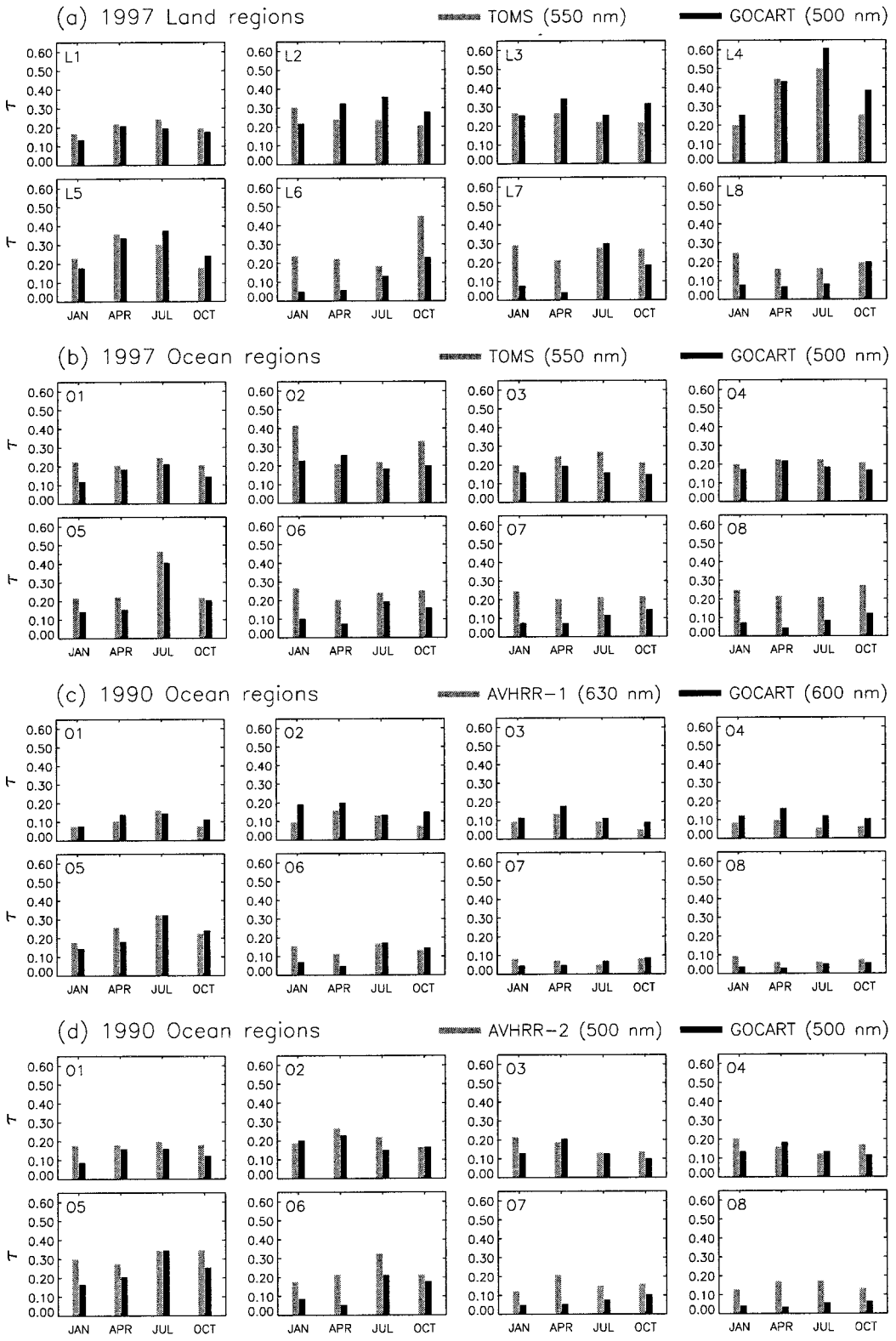

FIG. 9. Regional comparisons of modeled and satellite retrieved aerosol optical thickness for the same period of time as in Figs. 6 and 7: (a) TOMS over the land regions; (b) TOMS over the oceanic regions. (c) AVHRR-1 over the oceanic regions; and (d) AVHRR-2 over the oceanic regions. Borders of each region are indicated in Fig. 8. See text for descriptions of the regions.

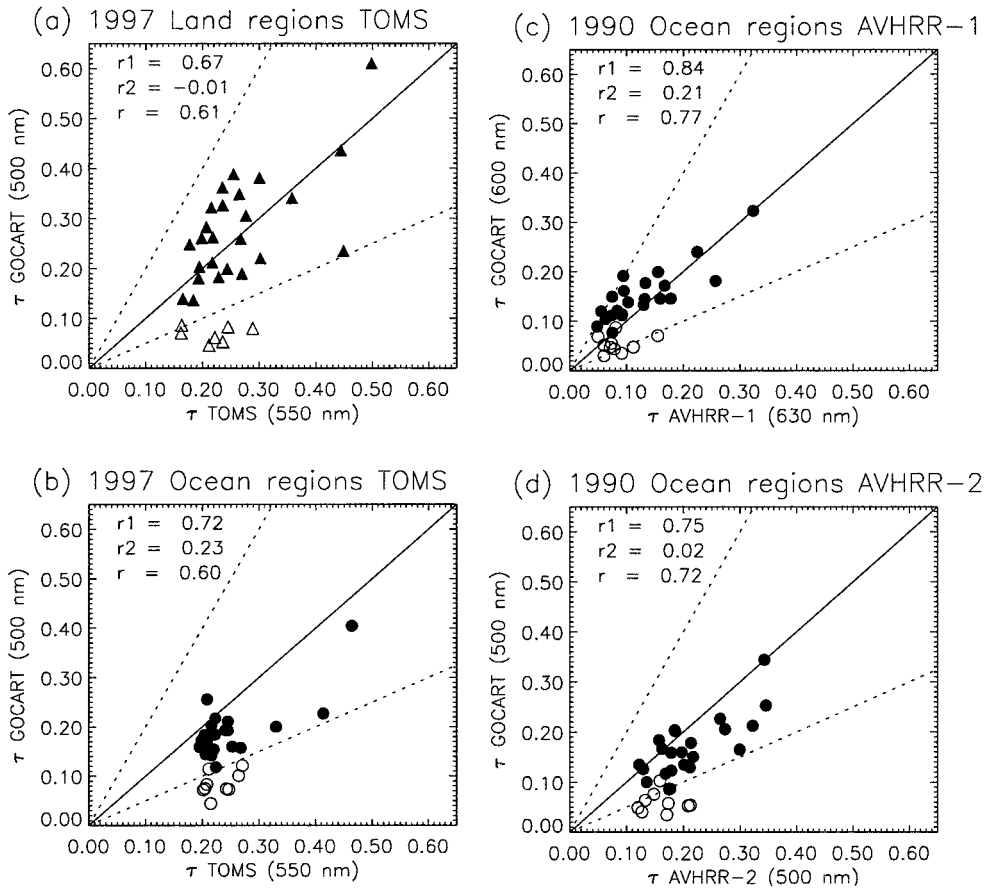

FIG. 10. Scatterplots of modeled vs satellite retrieved τs from Fig. 9: (a) TOMS over the land regions; (b) TOMS over the oceanic regions; (c) AVHRR-1 over the oceanic regions; and (d) AVHRR-2 over the oceanic regions. See text and Fig. 8 for descriptions of the regions. Solid line is the 1:1 ratio, and dotted lines are a factor of 2 departure. Solid symbols are for either the land source (triangle) or outflow (circle). Open symbols are for either land regions without significant emission (triangle) or remote ocean (circle). Correlation coefficient r1 is for solid symbols, r2 for open symbols, and r for all points.

in January but 20°N in July. Among the model studies that had tried to explain this shift, Tegen and Fung (1995) suggested that emission from human disturbed soil was necessary to reproduce the satellite observed peak location in January, whereas Takemura et al. (2000) argued that it was the combination of carbonaceous aerosol from biomass burning and dust aerosol that caused the apparent seasonal shift. We plot in Fig. 11 the latitudinal variation of τ from our model along with that from the AVHRR-2 at 22.5°W longitude transect in January and July of 1990. The τs for individual aerosol types from the model are superimposed. The model reproduces the observed seasonal shift of maximum τ, though the peak value in January is only about half of that from AVHRR-2. The peak is located at 5°–10°N in January, a season when biomass burning in northern Africa is the most active. The model results suggest that carbonaceous aerosol from biomass burning contributes the most to the maximum τ at this location, but the contribution from dust is also important. This conclusion is consistent with the study by Takemura et al. (2000). A close look at Fig. 11 reveals that the modeled dust at 0°–30°N consists of two peaks, one at 18°–20°N, which originates mainly from the western Sahara (Mauritania and Mali) region, while the other at 8°–10°N, which originates from the Lake Chad–Bodele depression in the Sahel region (Ginoux et al. 2001). In contrast, in July the peak of τ is shifted to 20°N, and dust is the predominant aerosol contributing to the maximum τ. Compared to January, the τ is low at latitudes south of 10°N, because there is little biomass burning activity in that season and aerosols are washed out by the moisture and precipitation brought by the northward migrating intertropical convergence zone. Next to dust, sulfate aerosol transported from Europe contributes to nearly 20% of the peak values of τ in July. The AVHRR-2 data in Fig. 11 also show an increase of τ with latitudes from 30° to 60° in both hemispheres. The model results agree with such a latitudinal variation, which is controlled by sea salt aerosols except in July at the Northern Hemisphere where sulfate and dust are more important.

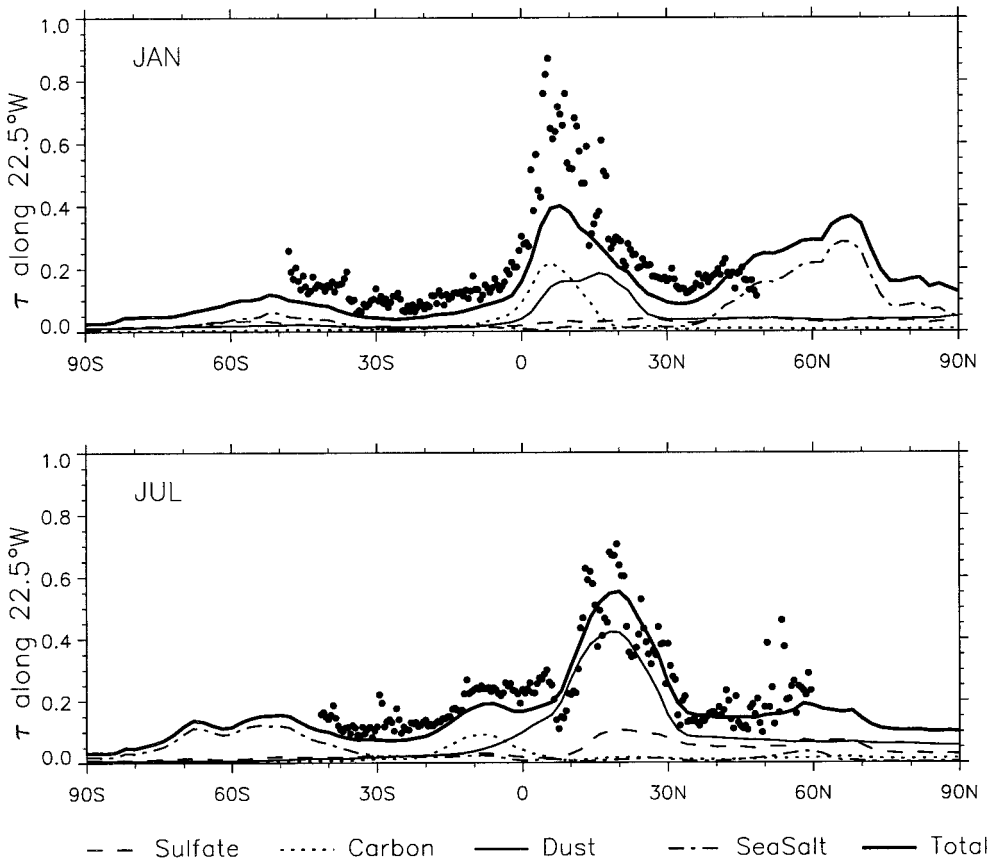

FIG. 11. Latitudinal variation of total τ from the model (thick line) and from the AVHRR (closed circle) along 22.5°W longitude in Jan and Jul 1990. The modeled τs from individual aerosol components are also shown.

6. Comparison with ground-based sun photometer measurements from AERONET

The AERONET program is a federation of the ground-based sun photometer measurement network (Holben et al. 1998), which started in 1993 at more than a dozen sites, has grown rapidly to over 100 sites worldwide (Holben et al. 2001). The AERONET has been providing column-integrated aerosol optical properties at 8 wavelengths from 340 to 1020 nm. Data from AERONET measurements have been used for satellite and model validation (Kinne et al. 2001; Torres et al. 2002; Zhao et al. 2002). Here we compare our model results with the AERONET measurements of τ at 500 nm at 20 sites (locations shown in Fig. 12), where the data are quality-assured with 2 or more yr of measurements available (Holben et al. 2001).

The comparisons are shown in Fig. 13. The period of AERONET measurements varies with sites, as indicated in Fig. 13, while the model results are the average of 1996 and 1997, a period that has been included in most of the AERONET measurement sites. The first four sites in Fig. 13 are predominantly influenced by biomass burning aerosols: Mongu in southern Africa; Cuiaba, Los Fieros, and Brazilia in Brazil. The model shows that the biomass burning activity peaks in September at these four sites, consistent with the AERONET measurements. The model-simulated seasonal variation has improved significantly from the previous studies (see Chin et al. 2001) because of a more realistic biomass burning emission dataset used in this study (section 2d). However the magnitude of the maximum τ at three South American sites is underestimated in the model by a factor of 2–3, suggesting that the biomass burning emission in the model is probably too low in Brazil during the burning season.

Sites 5–8 in Fig. 13 are located in northern Africa and are influenced by both dust aerosol and carbonaceous aerosol from biomass burning. The relative importance of these two types of aerosol depends on the season. In winter months the carbonaceous aerosol is important and stands as the major aerosol type at site 5 and 6, while dust aerosol dominates the remainder of the year. The model results are consistent with the Ångström parameters (α) from the AERONET. For example, at Banizoumbo, aerosol particle sizes were small (α = 1.5) during December, January, and February, consistent with the characteristics of smoke aerosols; but were large (α = 0.2–0.5) in other months, consistent with the

characteristics of dust aerosols (Holben et al. 2001). However, the modeled τs are too low in springtime at these sites, although in general they still rest within the standard deviations of the data. The strong perturbation over the local dust source, which is not resolved in the model, might explain the discrepancies (Ginoux et al. 2001).

Aerosols in sites 9–12 in Fig. 13 consist mainly of mineral dust: Dalanzadgad located in the Gobi Desert, Bahrain and Sede Boker in the Middle East, and Cape Verde off the west coast of northern Africa. The model overestimates τ at Dalanzadgad from April to December, a problem that may be related to the possibility that too large a fraction of small dust particles ($r_e \leq 1.5$ μm) have been emitted from the Taklimakan and Gobi Deserts (Ginoux et al. 2001). Consequently, the amount of dust being transported out from Asia may be overestimated because smaller dust particles have longer lifetime and are subject to more efficient long-range transport than larger particles (Ginoux et al. 2001). The model reproduces closely the observed seasonal variation at Bahrain, Sede Boker, and Cape Verde, although the modeled τ values are 20%–40% higher than the AERONET data at the former two sites.

Sites 13–16 are generally considered as being dominated by pollution aerosols: Ispra in Italy, Goddard Space Flight Center at suburban Washington D.C., Bondville in Illinois, and the Cloud and Radiation Testbed site in Oklahoma. The model results do show that sulfate aerosol from anthropogenic sources is a major component at these sites, followed by dust aerosol. Despite the fact that the calculated τ values are within the uncertainty range of the observations, high α (1.0–1.8) from the AERONET retrieval indicates that aerosols at these sites are mainly composed by small particles (Holben et al. 2001) rather than dust. This suggests that the background level of dust aerosol in the model is probably too high.

The last four sites in Fig. 13 contain various aerosol types. The model results show that at Bermuda and Dry Tortugas, dust is the major aerosol type, mainly from the long-range transport from Africa, while in winter and early spring other aerosol types are equally important. The model misses the spring maximum as shown in the AERONET data at these two sites. The seasonal variation of τ at Sevilleta is simulated by the model, with dust as a primary source in the spring and sulfate in the summer, though the τ is a factor of 2 too high in the model. Finally, at the oceanic site of Lanai (Hawaii), the modeled τ values are too high, especially from May to October, a bias that can be partly attributed to the possible overestimate of small dust particle emissions from Asia, as seen at Dalanzadgad (site 9). The small particles can be efficiently uplifted to 7–8-km altitude and subsequently transported to large areas over the North Pacific Ocean (Ginoux et al. 2001).

Figure 14 is the scatterplot of all the data points in Fig. 13 showing the degree of agreement between the model and AERONET data. In most cases, the model and AERONET agree within a factor of 2, with an overall correlation coefficient of 0.70. The model has a tendency to overestimate the τ at low aerosol levels, probably due to the overestimation of the background dust level. On the other hand, the model tends to underestimate the τ when aerosol loadings are high, such as during the biomass burning season in Brazil and springtime in Sahel region in northern Africa, suggesting the model has either too-low emission rates or too-coarse resolution to capture the subgrid characteristics.

7. Discussion

In comparing the τ calculated from the model with that from the TOMS and AVHRR products (section 5), we have shown that the model and the satellite data have a broad agreement over the land source regions and neighboring oceans, and that the model reproduces the most prominent features in global distributions of τ from the satellite data. However, quantitative interpretations are still limited to regions where τs are high and where, preferably, one aerosol type dominates, such as dust or biomass burning regions. Outside these regions, it is difficult to use satellite data to constrain the model or use the model to interpret the data. This is because large uncertainties are involved in deriving the τs from both the model and satellite measurements, of which we will discuss a few here. Since these uncertainties exist in most global models and generally in all satellite retrievals, our considerations here are not limited to the GOCART model or the three satellite datasets used in this study.

From the modeling point of view, there are two quantities in Eq. (2) that determine the τ at any given wavelengths: dry aerosol mass M_d and the mass extinction efficiency β. The aerosol dry mass M_d is determined by the sources, transport, and removal processes, and uncertainties in these processes will affect model results in terms of the amount and distributions of aerosol dry mass. The parameters used to estimate the sources, for example, biomass emission factors, threshold velocity of dust erosion, wind-dependent sea salt flux function, and biogenic OC emission, are still highly uncertain. It has been shown that globally, M_d and τ are almost linearly related to the emissions of individual aerosol types or their precursors (Chin et al. 2001). Errors in aerosol emission will therefore have a direct effect on model-calculated M_d and τ. Even with the same prescribed emission rates, the previous model intercomparisons showed that models differ by at least a factor of 2 on column burden, although they usually agree relatively well with each other on surface concentrations (Barrie et al. 2001; Penner et al. 2002), a discrepancy that reflects uncertainties in transport and removal rates. On the other hand, given the simulated dry mass, the quantity of β for each type of aerosol is determined by the microphysical and optical properties, that is, hygro-

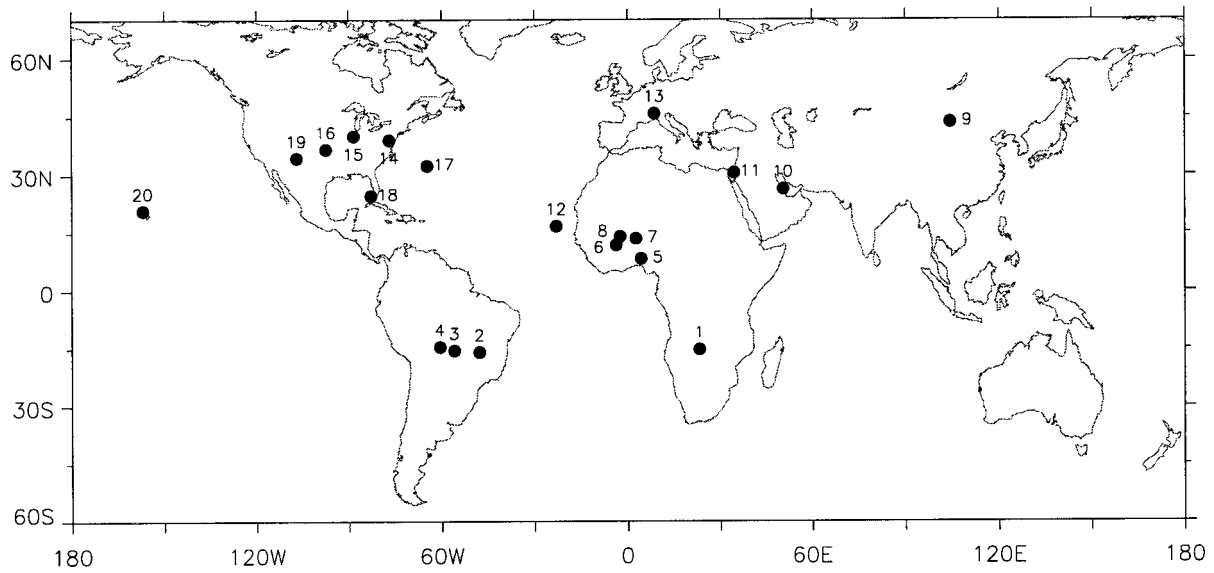

FIG. 12. Locations of 20 AERONET sites. The latitude, longitude, and names of these sites are shown in Fig. 13.

scopic growth rates, size distributions, and refractive indices. At the present time these properties are highly parameterized based on quite limited measurements. One example is the refractive index for dust aerosols. Depending on the mineralogical composition, the optical property of dust could vary significantly from highly absorbing to highly scattering (Sokolik and Toon 1999). The composition is likely to change from one location (e.g., the Sahara) to another (e.g., the Taklimakan). However, the model does not take into account the difference in mineral composition and instead uses a ''universal'' optical refractive index for all dust. Also difficult is the treatment of aerosol mixing state, that is, the degree of internal mixing in an environment where two or more types of aerosol exist. Without the observation-based parameters describing the mixing state under different environmental and meteorological conditions, it is not possible to accurately model the mixing state at the global scale.

As for satellite retrieval, crucial uncertainties are also inherent. In order to derive the τ from the measured radiance, assumptions have to be made in the retrieval process with respect to cloud fraction, surface reflectance, aerosol type, size distributions, complex refractive indices, and, in some cases, the aerosol layer height. One of the largest uncertainties in satellite retrieval is cloud screening. For example, Mishchenko et al. (1999) demonstrated that different methods used for cloud screening in the AVHRR retrieval could lead to 0.1 or larger differences in τ values over the oceans. Because there are no concurrent cloud measurements from the TOMS satellite platform, a reflectivity threshold has to be used in the TOMS retrieval to reject those data pixels that are obviously contaminated by clouds (see Table 4). However, thin clouds may not be screened out, which poses the largest problem in the TOMS retrieval and leads to an overestimate of aerosol τ (Torres et al. 1998; 2002). This problem is especially serious over remote regions where aerosol is optically thin. In fact, it has been pointed out that the TOMS retrieval is not sensitive to low aerosol amounts ($\tau = 0.2$ or lower at 550 nm; Torres et al. 2002). In addition, differences in the assumptions of aerosol type, particle shape, and size distributions applied in different retrieval algorithms also raise the level of uncertainties. As we have shown in section 5 and Figs. 7 and 9, the two different methods could result in a factor of 2 difference in the τs retrieved from the same AVHRR radiance data.

Apart from the sources of uncertainty in producing aerosol optical thickness by the model or by the satellite retrieval alone, model results and satellite products are often compared in an inconsistent manner. First, the satellite products contain only ''cloud free'' data, whereas the model results are not cloud-screened. Rejecting the cloudy or partially cloudy pixels could cause the satellite data to be biased low because most secondary aerosols (sulfate) are formed in clouds and the hygroscopic growth is most effective at high humidity regions near the clouds. However, it could also cause the satellite data to be biased high because aerosol scavenging by clouds and precipitation is an important removal mechanism of aerosols. Second, the microphysical and optical parameters used in the satellite retrieval are usually not the same as the ones used in the model, as we have seen in Table 2 (model) and Table 4 (satellite). Furthermore, neither TOMS nor AVHRR retrievals consider the effects of relative humidity on aerosol particle sizes and refractive indices. As a result, the τ values derived from the satellite and from the model are based on different assumptions of the physical and optical parameters, so that the link between the model and the satellite data at the present stage can only be defined as qualitative or

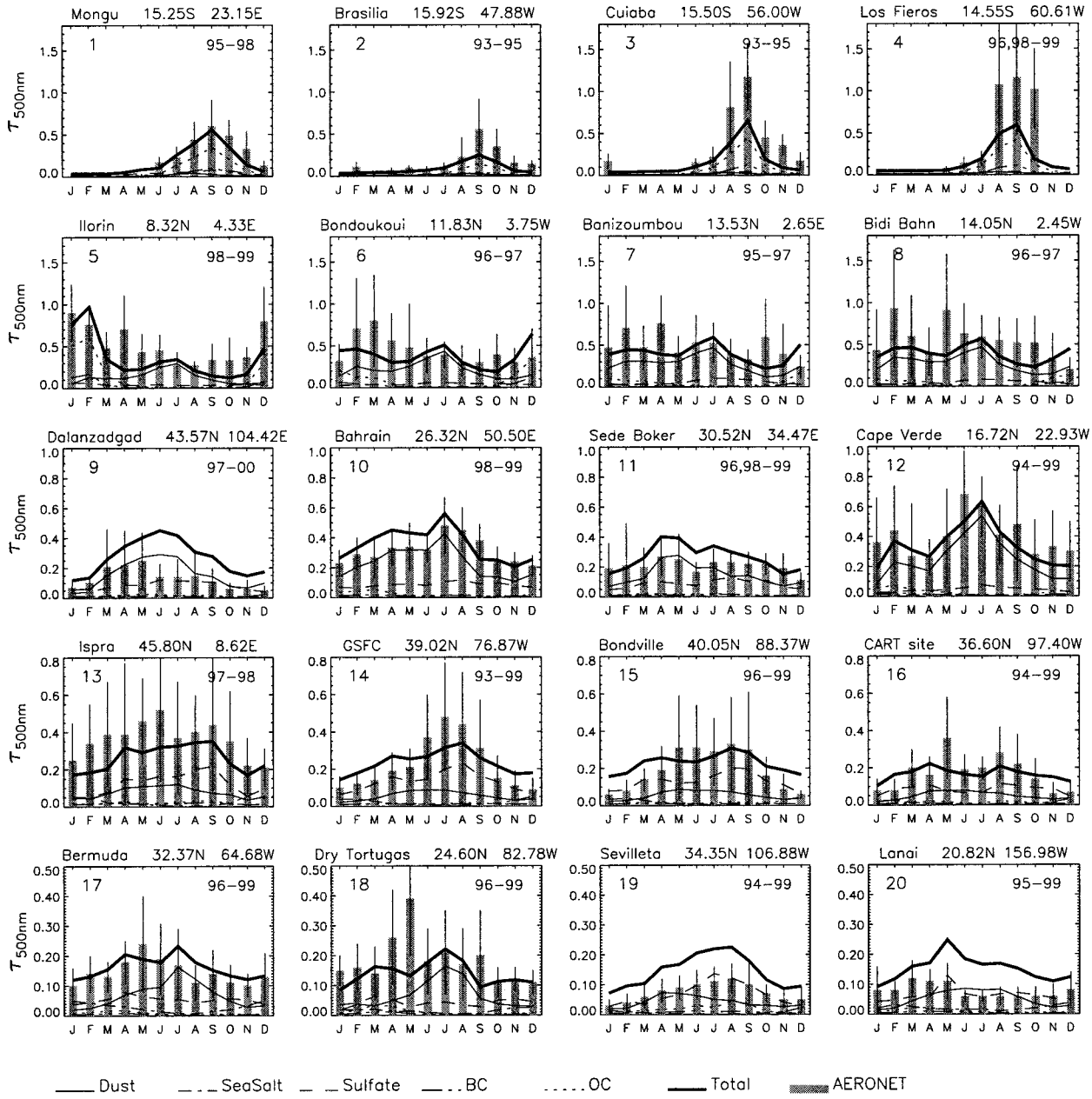

FIG. 13. Comparison of total aerosol optical thickness calculated in the model (thick line) with that measured at 20 AERONET sites (vertical bar). Site number as labeled in Fig. 12 and the measurement period are indicated for each site. Model results are 2-yr averaged values of 1996–97.

semiquantitative. More effort should then be made to study the sensitivity of the τ to the parameters and methods used in the model and in the satellite retrieval.

The ground-based AERONET program plays a pivotal role in offering a benchmark for satellite and model validation. The AERONET data are especially useful as they provide comprehensive measurements of aerosol properties including τ, Ångström parameter (Holben et al. 2001), and, more recently, single scattering albedo and size distribution (Dubovik et al. 2002). However, caution should be exercised in model evaluations because all the AERONET data, similar to the satellite measurements, are only daytime samples under cloud-free conditions. In addition, because the AERONET data are from point measurements, they may not always be representative of the model gridbox that is usually in a spatial scale of a few hundreds of km resolution. Another limitation of the AERONET data is that they cannot provide information on chemical composition and aerosol vertical profile, which are among the largest uncertainties in model simulation. Nonetheless, the comprehensive AERONET dataset should provide a wide range of constraints to check the model performance. We

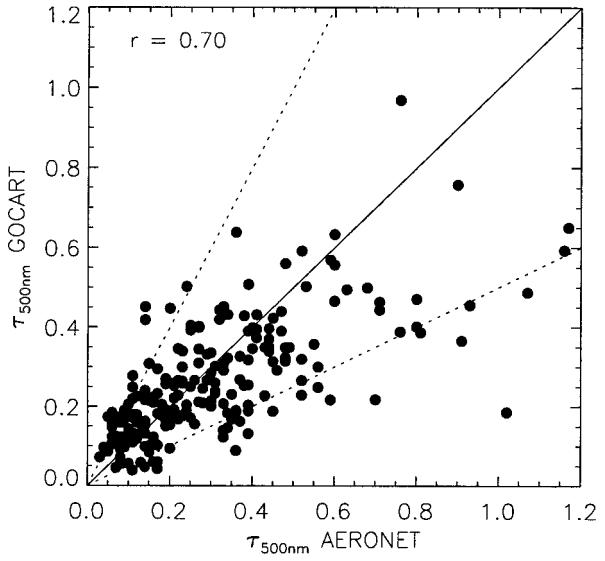

FIG. 14. Scatterplot of modeled vs AERONET observed τs from Fig. 13. Solid line is the 1:1 ratio, and dotted lines are a factor of 2 departure.

will extend our comparisons to other AERONET aerosol property data, in addition to τ, in our future work.

8. Conclusions

We have used the GOCART model to simulate the aerosol optical thickness for major types of tropospheric aerosols including sulfate, dust, OC, BC, and sea salt. The GOCART model uses a dust emission algorithm that quantifies the dust source as a function of the degree of topographic depression, and a biomass burning emission source that includes seasonal and interannual variability based on the satellite observations. These physically and observationally based aerosol emissions, along with the use of assimilated meteorological fields, have made the model suitable for comparisons with observations conducted at a wide range of spatial and temporal scales.

Using the simulated aerosol mass and the GADS microphysical and optical data, we have calculated the optical thickness for individual aerosol types as a function of ambient relative humidity. Our results have shown that the globally averaged τ in 1990 at 500 nm is 0.040 for sulfate, 0.017 for OC, 0.007 for BC, 0.051 for dust, and 0.027 for sea salt, corresponding to the mass extinction efficiency β of 10.3, 6.8, 12.2, 0.8, and 1.0 $m^2 g^{-1}$, respectively. However, there are large spatial and temporal variations of τ and β, determined mainly by the emission, transport, particle size, and the hygroscopic growth rates of aerosol.

Model-calculated τs have been compared with the most recent satellite products from the TOMS retrieval over both land and ocean and with both one- and two-channel retrieval products from the AVHRR over the ocean. The model reproduces the prominent features of geographical and temporal variations of τs as observed by the satellites, such as dust plumes over northern Africa and the Arabian Peninsula, biomass burning plumes in southern Africa, the intense biomass burning signal over Indonesia in October 1997, sea salt band at high latitudes, and the seasonal shift of the latitudinal locations of the aerosol plume off the west coast of northern Africa. While there are clear differences among the satellite products, a major discrepancy between the model and the satellite data is that the model shows a much stronger variation of τ from source to remote regions. The model results and the satellite data agree to within a factor of 2 over the aerosol source and outflow regions, but they are typically a factor of 2–5 lower than the TOMS and the two-channel AVHRR retrieval data over the remote regions or under background conditions. Cloud contamination and the low sensitivity at low aerosol levels in the satellite retrieval are likely the main causes of the discrepancy, although we cannot exclude the possibility that the sources, such as sea salt emission, are severely underestimated in the model in the remote regions.

The comparisons of model results with the data from the AERONET sites have shown that the model reproduces the seasonal variations at most of the sites, especially the places where biomass burning or dust aerosol dominate, even though the magnitudes do not always match the observations. At areas near or influenced by the Asian dust source, the modeled τ is too high, which may be attributed to an overestimate of the fraction of small dust particle emissions from the Asian desert followed by efficient long-range transport to large areas over the North Pacific.

We have also discussed the difficulties and problems in quantitative comparison of model results with the satellite data, caused by large uncertainties involved in deriving the τs by both the model and satellite retrieval. For models, the uncertainties include processes associated with the simulation of aerosol mass (emission, chemistry, transport, and removal) and parameters used in calculating the mass extinction efficiency (hygroscopic properties, refractive indices, and mixing state). For satellite retrievals, the uncertainties involve the cloud screen method, surface reflectance, and assumptions in aerosol properties. Furthermore, there are inconsistencies between the model and satellite retrieval in terms of the exclusion of clouds, assumption of aerosol types, and microphysical and optical parameters in deriving the τ values. At present, the comparison of the model and satellite results can be meaningfully interpreted only in regions where the τs are high and dominated by one type of aerosol, such as the near-African dust source area or intensive biomass burning regions. More effort should be made to study the sensitivity of the τ to the uncertainties in the model and in the satellite retrieval. Finally, more comprehensive comparisons with the AERONET measurements of aerosol properties and closely coordinated investigations between mod-

eling, field experiments, and satellite retrieval should be pursued to reduce these uncertainties.

Acknowledgments. We thank Larry Stowe and the NOAA Satellite Active Archive for providing the one-channel AVHRR retrieval products of aerosol optical thickness, and William Cooke for providing the anthropogenic emission inventory for OC and BC emissions. We thank the principal investigators and field managers Didier Tanre, Rachel Pinker, Chuck McClain, Giuseppe Zibordi, Rangasayi Nalthore, Ken Voss, John V. Castle, Bernadette Chatenet, Francois Lavenu, and the AERONET program team for providing the ground-based aerosol data used in this work. This work is supported by the NASA Global Aerosol Climate Project (GACP) and Atmospheric Chemistry Modeling and Analysis Program (ACMAP). Randall Martin was supported by a National Defense Science and Engineering Graduate (NDSEG) Fellowship. Comments from two anonymous reviewers are gratefully acknowledged.

REFERENCES

Allen, D. J., P. Kasibhatla, A. M. Thompson, R. B. Rood, B. G. Doddridge, K. E. Pickering, R. D. Hudson, and S.-J. Lin, 1996: Transport-induced interannual variability of carbon monoxide determined using a chemistry and transport model. *J. Geophys. Res.*, **101,** 28 655–28 669.

Andreae, M. O., and Coauthors, 1988: Biomass-burning emissions and associated haze layers over Amazonia. *J. Geophys. Res.*, **93,** 1509–1527.

Andres, R. J., and A. D. Kasgnoc, 1998: A time-averaged inventory of subaerial volcanic sulfur emissions. *J. Geophys. Res.*, **103,** 25 251–25 261.

Arino, O., and J.-M. Melinotte, 1995: Fire index atlas. *Earth Obs. Quart.*, **50,** 11–16.

——, and J.-M. Rosaz, 1999: 1997 and 1998 World ATSR Fire Atlas using ERS-2 and ATSR-2 data. *Proc. Joint Fire Science Conf*., Boise, ID, University of Idaho and International Association of Wildland Fire, 177–182.

Atlas, R., R. N. Hoffman, S. C. Bloom, J. C. Jusem, and J. Ardizzone, 1996: A multiyear global surface wind velocity dataset using SSM/I wind observations. *Bull. Amer. Meteor. Soc.*, **77,** 869–882.

Balkanski, Y. J., D. J. Jacob, G. M. Gardner, W. C. Graustein, and K. K. Turekian, 1993: Transport and residence times of tropospheric aerosols inferred from a global three-dimensional simulation of 210Ph. *J. Geophys. Res.*, **98,** 20 573–20 586.

Barrie, L. A., and Coauthors, 2001: A comparison of large scale atmospheric sulphate aerosol models (COSAM): Overview and highlights. *Tellus*, in press.

Bluth, G. J. S., W. I. Rose, I. E. Sprod, and A. J. Krueger, 1997: Stratospheric loading of sulfur from explosive volcanic eruptions. *J. Geol.*, **105,** 671–683.

Chin, M., R. B. Rood, S.-J. Lin, J.-F. Muller, and A. M. Thompson, 2000a: Atmospheric sulfur cycle simulated in the global model GOCART: Model description and global properties. *J. Geophys. Res.*, **105,** 24 671–24 687.

——, and Coauthors, 2000b: Atmospheric sulfur cycle simulated in the global model GOCART: Comparison with field observations and regional budgets. *J. Geophys. Res.*, **105,** 24 689–24 712.

——, P. Ginoux, B. Holben, M.-D. Chou, S. Kinne, and C. Weaver, 2001: The GOCART model study of aerosol composition and radiative forcing. Preprints, *12th Symp. on Global Change and Climate Variations*, Albuquerque, NM, Amer. Meteor. Soc., J1–J6.

Cooke, W. F., and J. J. N. Wilson, 1996: A global black carbon aerosol model. *J. Geophys. Res.*, **101,** 19 395–19 409.

——, C. Liousse, H. Cachier, and J. Feichter, 1999: Construction of a $1° \times 1°$ fossil fuel emission data set for carbonaceous aerosol and implementation and radiative impact in the ECHAM4 model. *J. Geophys. Res.*, **104,** 22 137–22 162.

d'Almeida, G. A., 1991: *Atmospheric Aerosols.* A. Deepak Publishing, 561 pp.

Dubovik, O., B. Holben, T. F. Eck, A. Smirnov, Y. J. Kaufman, M. D. King, D. Tanré, and I. Slutsker, 2002: Variability of absorption and optical properties of key aerosol types observed in worldwide locations. *J. Atmos. Sci.*, **59,** 590–608.

Fuchs, N. A., 1964: *The Mechanics of Aerosols.* Pergamon Press, 408 pp.

Ginoux, P., M. Chin, I. Tegen, J. Prospero, B. Holben, O. Dubovik, and S.-J. Lin, 2001: Sources and distributions of dust aerosols simulated with the GOCART model. *J. Geophys. Res.*, **106,** 20 225–20 273.

Giorgi, F., and W. L. Chameides, 1986: Rainout lifetimes of highly soluble aerosols and gases as inferred from simulations with a general circulation model. *J. Geophys. Res.*, **91,** 14 367–14 376.

Gong, S., L. A. Barrie, and J.-P. Blanchet, 1997: Modeling sea salt aerosols in the atmosphere. 1: Model development. *J. Geophys. Res.*, **102,** 3805–3818.

Grim, R. E., 1968: *Clay Mineralogy*. McGraw-Hill.

Guenther, A., and Coauthors, 1995: A global model of natural volatile organic compound emissions. *J. Geophys. Res.*, **100,** 8873–8892.

Hansen, J. E., and L. D. Travis, 1974: Light scattering in planetary atmospheres. *Space Sci. Rev.*, **16,** 527–610.

Haywood, J. M., D. L. Roberts, A. Slingo, J. M. Edwards, and K. P. Shine, 1997: General circulation model calculations of the direct radiative forcing by anthropogenic sulfate and fossil-fuel soot aerosol. *J. Climate*, **10,** 1562–1577.

Helfand, H. M., and J. C. Labraga, 1988: Design of a nonsingular level 2.5 second-order closure model for the prediction of atmospheric turbulence. *J. Atmos. Sci.*, **45,** 113–132.

Herman, J. R., and E. A. Celarier, 1997: Earth surface reflectivity climatology et 340 nm to 380 nm from TOMS data. *J. Geophys. Res.*, **102,** 28 003–28 011.

——, P. K. Bhartia, O. Torres, C. Hsu, C. Seftor, and E. Celarier, 1997: Global distribution of UV-absorbing aerosols from Nimbus-7/TOMS data. *J. Geophys. Res.*, **102,** 16 911–16 922.

Higurashi, A., T. Nakajima, B. N. Holben, A. Smirnov, R. Frouin, and B. Chatenet, 2000: A study of global aerosol optical climatology with two-channel AVHRR remote sensing. *J. Climate*, **13,** 2011–2027.

Holben, B. N., and Coauthors, 1998: AERONET—A federated instrument network and data archive for aerosol characterization. *Remote Sens. Environ.*, **66,** 1–16.

——, and Coauthors, 2001: An emerging ground-based aerosol climatology: Aerosol optical depth from AERONET. *J. Geophys. Res.*, **106,** 12 067–12 098.

Houghton, J. T., L. G. Meira Filho, J. Bruce, Hoesung Lee, B. A. Callander, E. Haites, N. Harris, and K. Maskell, Eds., 1995: *Climate Change 1994: Radiative Forcing of Climate Change and An Evaluation of the IPCC IS92 Emission Scenarios.* Cambridge University Press, 339 pp.

Kettle, A. J., and Coauthors, 1999: A global database of sea surface dimethylsulfide (DMS) measurements and a simple model to predict sea surface DMS as a function of latitude, longitude, and month. *Global Biogeochem. Cycles*, **13,** 399–344.

Kinne, S., and Coauthors, 2001: How well do aerosol retrievals from satellites and representations in global models match ground-based AERONET aerosol statistics? *Remote Sensing and Climate Modeling: Synergies and Limitations*, M. Beniston and M. M. Verstratete, Eds., Kluwer Academic, 103–158.

Köpke, P., M. Hess, I. Schult, and E. P. Shettle, 1997: Global aerosol data set. Tech. Rep. 243, Max-Planck Institute, 44 pp.

Kotchenruther, R. A., P. V. Hobbs, and D. A. Hegg, 1999: Humidification factors for atmospheric aerosols off the mid-Atlantic coast of the United States. *J. Geophys. Res.*, **104,** 2239–2251.

Lacis, A. A., and M. I. Mishchenko, 1994: Climate forcing, climate

sensitivity, and climate response: A radiative modeling perspective on atmospheric aerosols. *Aerosol Forcing of Climate*, R. J. Charlson and J. Heintzenberg, Eds., John Wiley and Sons, 416 pp.

Li-Jones, X., H. B. Maring, and J. M. Prospero, 1998: Effect of relative humidity on light scattering by mineral dust aerosol as measured in the marine boundary layer over the tropical Atlantic Ocean. *J. Geophys. Res.*, **103,** 31 113–31 121.

Lin, S.-J., and R. B. Rood, 1996: Multidimensional flux-form semi-Lagrangian transport schemes. *Mon. Wea. Rev.*, **124,** 2046–2070.

Liousse, C., J. E. Penner, C. Chuang, J. J. Walton, H. Eddleman, and H. Cachier, 1996: A global three-dimensional model study of carbonaceous aerosols. *J. Geophys. Res.*, **101,** 19 411–19 432.

Liss, P. S., and L. Merlivat, 1986: Air–sea gas exchange rates: Introduction and synthesis. *The Role of Air–Sea Exchange in Geochemical Cycling*, P. Buat-Ménard, Ed., D. Riedel, 113–127.

Lobert, J. M., W. C. Keene, J. A. Logan, and R. Yevich, 1999: Global chlorine emissions from biomass burning: The reactive chlorine emissions inventory. *J. Geophys. Res.*, **104,** 8373–8390.

Mishchenko, M. I., I. V. Geogdzhayev, B. Cairns, W. B. Rossow, and A. A. Lacis, 1999: Aerosol retrievals over the ocean by use of channels 1 and 2 AVHRR data: Sensitivity analysis and preliminary results. *Appl. Opt.*, **38,** 7325–7341.

Monahan, E. C., D. E. Spiel, and K. L. Davidson, 1986: A model of marine aerosol generation via whitecaps and wave disruption. *Oceanic Whitecaps*, E. C. Monahan and G. Mac Niocaill, Eds., D. Reidel, 167–174.

Moulin, C., C. E. Lambert, F. Dulac, and U. Dayan, 1997: Control of atmospheric export of dust from North Africa by the North Atlantic Oscillation. *Nature*, **387,** 691–694.

Müller, J.-F., and G. Braseur, 1995: IMAGES: A three-dimensional chemical transport model of the global troposphere. *J. Geophys. Res.*, **100,** 16 445–16 490.

Nakajima, T., and A. Higurashi, 1998: A use of two-channel radiances for an aerosol characterization from space. *Geophys. Res. Lett.*, **25,** 3815–3818.

Olivier, J. G. J., and Coauthors, 1996: Description of EDGAR version 2.0: A set of global emission inventories of greenhouse gases and ozone-depleting substances for all anthropogenic and most natural sources on a per country basis and on $1^\circ \times 1^\circ$ grid. RIVM/TNO Rep. 771060-002. 140 pp.

Patterson, E. M., C. K. McMahon, and D. E. Ward, 1986: Absorption properties and graphitic carbon emission factors of forest fire aerosols. *Geophys. Res. Lett.*, **13,** 129–132.

Penner, J. E., and Coauthors, 2002: A comparison of model- and satellite-derived optical depth and reflectivity. *J. Atmos. Sci.*, **59,** 441–460.

Rao, C. R. N., L. L. Stowe, E. P. McClain, and J. Sapper, 1988: Development and application of aerosols remote sensing with AVHRR data from the NOAA satellites. *Aerosol and Climate*, P. V. Hobbs and M. P. McCormick, Eds., A. Deepak, 69–79.

Schubert, S. D., R. B. Rood, and J. Pfaendtner, 1993: An assimilated dataset for earth science applications. *Bull. Amer. Meteor. Soc.*, **74,** 2331–2342.

Simkin, T., and L. Siebert, 1994: *Volcanoes of the World.* 2d ed. Geoscience Press, 368 pp.

Sokolik, I. N., and O. B. Toon, 1999: Incorporation of mineralogical composition into models of the radiative properties of mineral aerosols from ultraviolet to infrared wavelengths. *J. Geophys. Res.*, **104,** 9423–9444.

Spiro, P. A., D. J. Jacob, and J. A. Logan, 1992: Global inventory of sulfur emissions with $1^\circ \times 1^\circ$ resolution. *J. Geophys. Res.*, **97,** 6023–6036.

Stowe, L. L., A. M. Ignatov, and R. R. Singh, 1997: Development, validation, and potential enhancements to the second-generation operational aerosol product at the National Environmental Satellite, Data, and Information Service of the National Oceanic and Atmospheric Administration. *J. Geophys. Res.*, **102,** 16 923–16 934.

Takemura, T., H. Okamoto, Y. Maruyama, A. Numaguti, A. Higurashi, and T. Nakajima, 2000: Global three-dimensional simulation of aerosol optical thickness distribution of various origins. *J. Geophys. Res.*, **105,** 17 853–17 873.

Tegen, I., and I. Fung, 1994: Modeling of mineral dust in the atmosphere: Sources, transport, and optical thickness. *J. Geophys. Res.*, **99,** 22 897–22 914.

——, and ——, 1995: Contribution to the mineral aerosol load from land surface modification. *J. Geophys. Res.*, **100,** 18 707–18 726.

——, and A. Lacis, 1996: Modeling of particle size distribution and its influence on the radiative properties of mineral dust aerosol. *J. Geophys. Res.*, **101,** 19 237–19 244.

——, P. Hollrig, M. Chin, I. Fung, D. Jacob, and J. Penner, 1997: Contribution of different aerosol species to the global aerosol extinction optical thickness: Estimates from model results. *J. Geophys. Res.*, **102,** 23 895–23 915.

Torres, O., P. K. Bhartia, J. R. Herman, Z. Ahmad, and J. Gleason, 1998: Derivation of aerosol properties from satellite measurements of backscattered ultraviolet radiation: Theoretical bases. *J. Geophys. Res.*, **103,** 17 009–17 110.

——, ——, ——, A. Sinyuk, P. Ginoux, and B. Holben, 2002: A long-term record of aerosol optical depth from TOMS observations and comparison to AERONET measurements. *J. Atmos. Sci.*, **59,** 398–413.

Wesely, M. L., 1989: Parameterization of surface resistance to gaseous dry deposition in regional-scale numerical models. *Atmos. Environ.*, **23,** 1293–1304.

Whitby, K. T., 1984: Behavior of sulfate-nitrate aerosols. *Hygroscopic Aerosols*, L. H. Ruhnke and A. Deepak, Eds., A. Deepak, 375 pp.

Zhao, T. X.-P., L. L. Stowe, A. Smirnov, D. Crosby, J. Sapper, and C. R. McClain, 2002: Development of a global validation package for satellite oceanic aerosol optical thickness retrieval based on AERONET observations and its application to NOAA/NESDIS operational aerosol retrievals. *J. Atmos. Sci.*, **59,** 294–312.